Chained structure of dimeric F_1-like ATPase in *Mycoplasma mobile* gliding machinery

Takuma Toyonaga[a], Takayuki Kato[b], Akihiro Kawamoto[b], Noriyuki Kodera[c], Tasuku Hamaguchi[a,d], Yuhei O Tahara[a,d], Toshio Ando[c], Keiichi Namba[e,f,g], Makoto Miyata[a,d,#]

[a]Graduate School of Science, Osaka City University, 3-3-138 Sugimoto, Sumiyoshi-ku, Osaka 558-8585, Japan.

[b]Institute for Protein Research, Osaka University, 3-2 Yamadaoka, Suita, Osaka, 565-0871, Japan.

[c]Nano Life Science Institute (WPI-NanoLSI), Kanazawa University, Kakuma-chou, Kanazawa, Ishikawa 920-1192, Japan.

[d]The OCU Advanced Research Institute for Natural Science and Technology (OCARINA), Osaka City University, 3-3-138 Sugimoto, Sumiyoshi-ku, Osaka 558-8585, Japan.

[e]Graduate School of Frontier Biosciences, Osaka University, 1-3 Yamadaoka, Suita, Osaka, 565-0871, Japan.

[f]RIKEN Center for Biosystems Dynamics Research and SPring-8 Center, 1-3 Yamadaoka, Suita, Osaka, 565-0871, Japan.

[g]JEOL YOKOGUSHI Research Alliance Laboratories, Osaka University, 1-3 Yamadaoka, Suita, Osaka, 565-0871, Japan.

[#]Address correspondence to Makoto Miyata, miyata@osaka-cu.ac.jp

Present address: Tasuku Hamagichi: Biostructural Mechanism Laboratory, RIKEN SPring-8 Center, 1-1-1 Kouto, Sayo, Hyogo, 679-5148, Japan.

Running title: Gliding machinery of *Mycoplasma mobile*

Keywords: F_1-ATPase, rotary motor, parasitic bacteria, electron microscopy, atomic force microscopy, bacterial motility

ABSTRACT

Mycoplasma mobile, a fish pathogen, exhibits gliding motility using ATP hydrolysis on solid surfaces, including animal cells. The gliding machinery can be divided into surface and internal structures. The internal structure of the motor is composed of 28 so-called 'chains' that are each comprised of 17 repeating protein units called 'particles'. These proteins include homologs of the catalytic α- and β-subunits of F_1-ATPase. In this study, we isolated the particles and determined their structures using negative-staining electron microscopy and high-speed atomic force microscopy. The isolated particles were composed of five proteins, MMOBs 1660 (α-subunit homolog), 1670 (β-subunit homolog), 1630, 1620, and 4530, and showed ATP hydrolyzing activity. The 2D structure, with dimensions of 35 and 26 nm, showed a hexameric ring dimer about 12 nm in diameter, resembling F_1-ATPase catalytic $(\alpha\beta)_3$. We isolated the F_1-like ATPase unit, which is composed of MMOBs 1660, 1670, and 1630. Furthermore, we isolated the chain and analyzed the 3D structure, showing that dimers of mushroom-like structures resembling F_1-ATPase were connected and aligned along the dimer axis at 31 nm intervals. An atomic model of F_1-ATPase catalytic $(\alpha\beta)_3$ from *Bacillus* PS3 was successfully fitted to each hexameric ring of the mushroom-like structure. These results suggest that the motor for *M. mobile* gliding shares an evolutionary origin with F_1-ATPase. Based on the obtained structure, we propose possible force transmission processes in the gliding mechanism.

54 **IMPORTANCE**

55 F_1F_o- ATPase, a rotary ATPase, is widespread in the membranes of mitochondria,
56 chloroplasts, and bacteria, and converts ATP energy with a proton motive force
57 across the membrane by its physical rotation. Homologous protein complexes play
58 roles in ion and protein transport. *Mycoplasma mobile*, a pathogenic bacterium,
59 was recently suggested to have a special motility system evolutionarily derived
60 from F_1-ATPase. The present study isolated the protein complex from *Mycoplasma*
61 cells and supported this conclusion by clarifying the detailed structures containing
62 common and novel features as F_1-ATPase relatives.

63 **INTRODUCTION**

64 Mycoplasmas are parasitic bacteria characterized by small cell size, a short
65 genome and lack of a peptidoglycan layer (1-3). Many *Mycoplasma* species exhibit
66 a unique gliding motility, which is necessary for their infection (4-6). *Mycoplasma*
67 *mobile* glides on solid surfaces at 2.0 to 4.5 μm/s in the direction of a protrusion on
68 one side of the cell (Fig. S1) (5). The gliding machinery is localized to the cell
69 protrusion and can be divided into surface and internal structures (Fig. 1A, upper).
70 The surface structure has approximately 450 repeats of a complex of three large
71 proteins, Gli123, Gli521, and Gli349, inserted into the cell membrane (Fig. 1A,
72 lower) (7-11). Fifty-nm-long leg structures corresponding to Gli349 molecules can
73 be seen jutting out from cell protrusion by electron microscopy (EM) (12). The tip of
74 Gli349 is characterized by a "foot" with an oval structure that can bind to sialylated
75 oligosaccharides (SOs) (13-20). Gli521 and Gli123 serve as the "crank" that
76 transfers force to Gli349 and the "mount" that localizes the other two surface
77 proteins to the gliding machinery, respectively. A working model of the gliding
78 mechanism has been proposed in which the cells are propelled by Gli349
79 molecules that repeatedly catch, pull, and release SOs on solid surfaces (5, 21-23).

80 The internal structure consists of a lumpy structure, called “bell” at the tip of the
81 cell protrusion and 28 “chains” lining the inner membrane surface (Fig. 1A) (23-26).
82 Each chain is characterized by 17 repeating particle structures, resulting in a total
83 of 476 particles in one cell. The chains tend to form sheets when they are isolated
84 from cells, suggesting lateral interaction with the adjacent chains (23, 24). The

85 internal structure consists of least ten proteins (Fig. 1B). Six of these proteins,
86 MMOBs 1620, 1630, 1640, 1650, 1660 and 1670 were coded tandemly in a locus.
87 Interestingly, MMOBs 1660 and 1670, which have Walker A and B motifs that are
88 involved in ATP binding and hydrolysis (27), show high amino acid sequence
89 identity with the catalytic subunits α and β of F_1-ATPase, respectively. MMOB1670
90 has an extra N-terminal region (amino acids 1–299), which is not present in the β
91 subunit. The chains most likely contain the motor for gliding, because the gliding
92 motility is coupled to ATP hydrolysis (23, 28, 29).

93 F_1F_o-ATPases, found in most organisms, are rotary motors that perform
94 biological energy conversion (30, 31). Their role is to both synthesize ATP using a
95 proton motive force and, conversely, to hydrolyze ATP to drive protons to maintain
96 the membrane potential. Their structure is composed of a soluble catalytic F_1-
97 domain for ATP catalysis and a membrane-embedded F_o-domain for the proton
98 pathway. In the F_1-domain, the catalytic subunits α and β alternate to form a
99 hexameric ring $(\alpha\beta)_3$ that rotates the central stalk penetrating the ring using ATP
100 hydrolysis. Phylogenetic studies have shown that *Mycoplasma* have three F_1-like
101 ATPase clusters, which are referred to as Type 1–3 ATPases (26, 32). Type 1,
102 found in all mycoplasmas, is a typical operon encoding F_1F_o-ATPase and is likely to
103 function as a proton pump to maintain membrane potential. Type 3 is found in
104 mycoplasmas that have an MIB-MIP system to cleave host immunoglobulins (33).
105 Type 2 is only found in four *Mycoplasma* species, including *M. mobile*. Interestingly,
106 the Type 2 ATPase of *M. mobile*, which encodes MMOB1620–70, is involved in the

107 internal structure of the gliding machinery.

108 Recently, the chains of the internal structure were shown to have structural
109 changes linked to ATP hydrolysis. However, it is still unclear how the chain
110 generates and transmits the force to the outside, because its detailed structure has
111 not been clarified. In this study, we isolated the chains and elucidated their
112 structures. The structure had a common architecture with F_1-ATPase, suggesting
113 that the chain shares a common evolutionary origin with F_1-ATPase. Based on our
114 findings, we suggest two possible force transmission models for the gliding
115 machinery.

116

117 **Results**

118 **Isolation and biochemical analyses of stable unit complex.** In this study,
119 we isolated and analyzed three fractions including “Dimer”, “Monomer”, and
120 “Chain” structures which are schematically shown in Fig. 1A (Fig. S2, S3).

121 First, to isolate a stable unit complex from the chain, we lysed cultured *M.*
122 *mobile* cells with 1% Triton X-100 and recovered the insoluble fraction by
123 centrifugation (24). This fraction named as “Pellet-1” was used for further
124 preparations. We suspended Pellet-1 in suspension buffer, which contains 137 mM
125 NaCl, and solubilized the putative unit complex for 8 h. Here, we used 137 mM
126 NaCl rather than 400 mM to reduce the contamination of other proteins. The
127 soluble fraction was then subjected to Superdex 200 gel filtration chromatography.

128 The obtained peak fraction in the void contained MMOBs 1620, 1630, 1660, and
129 1670, which are coded on the mycoplasma Type 2 ATPase operon, and
130 MMOB4530 annotated as phosphoglycerate kinase (PGK) (Fig. 2A). These
131 proteins are known to be components of the internal structure (Fig. 1B) (23-26).
132 To examine the assembly of these proteins, we applied the isolated fraction to
133 gel filtration chromatography using a Sephacryl S-400 HR column, which can
134 fractionate up to 8000 kDa globular proteins (Fig. 2B). The proteins eluted as a
135 single peak at a non-void position and were larger than 669 kDa, suggesting that
136 they form a large complex. The molar ratios of the components were estimated to
137 be 3.2:2.9:3.0:1.0:2.3 for MMOBs 1670, 4530, 1660, 1630, and 1620, respectively,
138 from the relative intensity of the SDS-PAGE bands. We then analyzed the isolated
139 fraction by blue-native (BN) PAGE (Fig. 2C, left). A single band was detected,
140 which is consistent with the result of gel filtration chromatography showing a single
141 peak. Next, we applied the band to an In-gel ATPase activity assay, which detects
142 the activity as a white precipitation of lead caused by released of inorganic
143 phosphate (Fig. 2C, right). The band with the complex showed precipitation,
144 whereas the band with thyroglobulin, the negative control, did not. This result
145 indicates that the isolated complex has ATPase activity.
146 In addition, we assayed the isolated fraction for phosphate release from
147 solution. The complex hydrolyzed ATP at a maximum turnover rate of 0.18
148 molecules/s per MMOB1670 subunit, β-subunit paralog with a K_m of 74 μM at 25°C
149 (Fig. 2D). The ATPase activity was inhibited by addition of 15.4 mM sodium azide,

150 an inhibitor to ATPases with Walker A motifs (35), with a K_m of 108 μM and a
151 maximum turnover rate of 0.055 molecules/s. In a previous study, the Triton-
152 insoluble fraction, which included the internal structure, showed ATPase activity
153 with a K_m of 66 μM and a maximum turnover rate of 0.09 molecules/s and was
154 suppressed by 15.4 mM sodium azide, showing a K_m of 84 μM and a maximum
155 rate of 0.063 molecules/s (23). The values obtained here are comparable to these
156 previous data. The above results suggest that the isolated complex is the motor in
157 the internal structure of the gliding machinery. We used this unit complex for further
158 analyses.

159 **Hexamers resembling F_1-ATPase catalytic $(\alpha\beta)_3$ form a dimer.** We
160 observed the unit complex by EM using the negative-staining method. A field image
161 showed uniform particles with dimensions of 40 and 20 nm (Fig. 3A and B). As the
162 particle frequency depended on the protein concentration, we concluded that the
163 observed particles were a part of the protein complex. We picked 2148 particle
164 images automatically using RELION software (36) for 2D-classification. From the
165 2D-classification, we obtained four clear particle images (Fig. S4). We adopted
166 mirror images according to the structure observed in high-speed atomic force
167 microscopy (HS-AFM) (see below). Structural handedness cannot be judged from
168 EM images because they are projections of electrons transmitted through the
169 sample. We focused on an image showing a complex structure with dimensions of
170 35 and 26 nm featuring nearly two-fold symmetry (Fig. 3C and D). Interestingly, the
171 characteristic hexamer of about 12 nm in diameter formed a dimer and was

172 reminiscent of F_1-ATPase catalytic $(\alpha\beta)_3$. Considering that the amino acid
173 sequences of MMOBs 1660 and 1670 have high identity to the α- and β-subunits of
174 F_1-ATPase, respectively, the dimeric complex is likely an evolutionary related F_1-
175 ATPase. The distance between the centers of the two hexamers was 11.0 nm. The
176 complex had ten filamentous structures around the two hexamers, four of which
177 appeared to form bridges across the two hexamers. The filamentous structures are
178 unlikely artifact, because they showed common features in four independent
179 averaged images (Fig. S4). Hereafter, we refer to this structural unit as "Dimer."
180 **The hexamer featured a ring and a peak in HS-AFM of Dimer.** Next, we
181 visualized Dimer using HS-AFM to clarify the structure under liquid conditions,
182 because the molecules are in dry condition under negative-staining EM. HS-AFM is
183 a powerful method that can visualize the structure and dynamics of single
184 molecules in liquid conditions at a video rate (37, 38). In this method, a specimen is
185 placed on the stage surface and with a probe is scanned in buffer at high speed. In
186 this study, we placed Dimer on a mica surface and scanned it in an area of 70 × 70
187 nm^2 at 56 × 56 pixels with a scanning rate of 100 ms per frame. HS-AFM images
188 showed a complex with dimensions of approximately 30 and 20 nm composed of
189 two globules and attached by 2–4 lateral protrusions shorter than 15 nm (Fig. 3E;
190 Movie S1 and S2). The Dimer images were categorized into two patterns as either
191 a ring (pattern I) or a peak (pattern II), based on the central part. Then, we
192 observed them at a higher resolution (area, 40 × 40 nm^2 with 50 × 50 pixels;
193 scanning rate, 100 ms per frame) (Fig. 3F). In pattern I, the slice image near the

194 top end of the particle between 9.8 and 11.3 nm above the substrate surface
195 showed two hexameric rings (Fig. 3G). The position and direction of the two rings
196 are consistent with those of the hexamers in the negative-staining EM image. In
197 addition, the distance between the centers of the two hexameric rings was 10.4 nm
198 (Fig. 3H), consistent with the distance between the centers of the hexamers in the
199 negative-staining EM image (Fig. 3C). These observations suggest that the shape
200 of the Dimer structure in liquid is preserved in negative-staining EM conditions and
201 that the hexamers form rings like F_1-ATPase catalytic $(\alpha\beta)_3$. In pattern II, the two
202 central peaks were positioned 11.2 nm apart (Fig. 3H, lower), similar to the
203 distance between the centers of the hexameric rings in pattern I (Fig. 3H, upper),
204 suggesting that patterns I and II are two sides of the same coin (Fig. 3E, left).
205 Interestingly, in most of the particles, the two peaks at 6 and 5 nm became invisible
206 in 20 s, between frames 1 and 3 (Fig. 3I and J; Movie S3). We concluded that
207 these subunits dropped out from the complex, because they did not reappear until
208 the complex was disrupted. Next, we focused on the lateral protrusions of these
209 particles, which may be related to the sheet formation of chains (23). To visualize
210 them more clearly, we scanned Dimer by HS-AFM with an area of 120 × 120 nm^2,
211 120 × 120 pixels, and scanning rate 500 ms per frame. Dimer showed seven lateral
212 protrusions around the two globules (Fig. 3K). These protrusions swayed without
213 being fixed (Fig. 3L; Movie S4).

214 **Isolation and structure of Monomer.** To clarify the components and structure
215 of the hexamer, we focused on the monomeric hexamer, called Monomer (Fig. S2).

216 We treated Dimer fraction with 1.5% sodium cholate, an anionic detergent. BN-
217 PAGE and In-gel ATPase activity assays showed a single band with ATPase
218 activity at a position lower than the original one, corresponding to 720–1048 kDa,
219 indicating that Dimer dissociated into smaller units with ATPase activity (Fig. 2C).
220 Therefore, to isolate Monomer, we applied Pellet-1 sequentially to the treatments
221 with 250 mM NaCl for 8 h, 1.5% sodium cholate for 7 h, and to Sephacryl S-400HR
222 gel filtration chromatography (Fig. S2). The elution pattern showed a rather isolated
223 small peak and following overlapping peaks (Fig. S3C). An SDS-PAGE gel showed
224 that MMOBs 1670, 1660, and 1630 eluted in the same fractions, while MMOBs
225 4530 and 1620 eluted at later fractions (Fig. S3CD), indicating that MMOBs 4530
226 and 1620 were dissociated from Dimer by sodium cholate treatment. Then, we
227 focused on the small peak fraction, which mainly contained MMOBs 1670, 1660,
228 and 1630 (Fig. 2A, middle, S3D). This complex presumably corresponds to the BN-
229 PAGE band showing ATPase activity (Fig. 2C), because only MMOBs 1660 and
230 1670 have the Walker A and Walker B motifs in the Dimer components. EM
231 observation using the negative-staining method showed uniform globular particles
232 10–15 nm in diameter (Fig. 4A and B). As the particle frequency depended on the
233 protein concentration, we concluded that the observed particles were a part of
234 Monomer. We picked 11687 particle images automatically using RELION software
235 for 2D-classification. By 2D-classifing the images in 50 classes, we obtained 15
236 clear particle images, which were averaged (Fig. S5). Fig. 4C shows a 12 nm
237 diameter globule characterized by a single hexameric ring, corresponding to a part

238 of the Dimer image in Fig. 3C. Three of the subunits were larger than the others
239 with hook structures on either side of the edge. Three averaged images (II–IV)
240 showed a mushroom-like structure resembling F_1-ATPase, which is characterized
241 by a 12 nm-diameter umbrella and a 3 nm-long stalk (Fig. 4C). Now, we can
242 suggest that MMOBs 1670, 1660, and 1630 form Monomer, i.e., F_1-like ATPase
243 unit. MMOB4530 was probably not included in this unit because it probably binds
244 to the complex and could not be distinguished in the image due to the low
245 proportion of bound entities (Fig. 2A, middle). Thus, the hexameric ring is likely
246 formed by the α-subunit homolog MMOB1660 and the β-subunit homolog
247 MMOB1670, and the stalk is formed by MMOB1630.

248 **Isolation and structure of Chain.** In gliding machinery, Dimer link to form
249 chains. To characterize these chains, we isolated "Chain fraction" with milder
250 mechanical treatment than those for other fractions. Pellet-1 was treated by 387
251 mM NaCl and soluble fraction was isolated. Chain fraction contained more than 30
252 proteins, including the Dimer component proteins MMOBs 1670, 4530, 1660, 1630,
253 and 1620 as major components (Fig. 2A, right). EM observation using the negative-
254 staining method showed chain structures with lengths longer than 70 nm and
255 particles of various sizes (Fig. 5A and B). This time we manually picked 2127
256 particles from the chain images, overlapping approximately 50% of the 71 × 71 nm^2
257 box area. From 2D-classifcation, we obtained seven clear particle images (Fig.
258 5C). The particle images show the various orientations required for 3D
259 reconstruction. We then created a 3D map by combining a total of 1709 particle

260 images of good quality (Fig. 5D and S6). The 3D map with dimensions of 70, 20,
261 and 15 nm at a density threshold (contour level = 0.026) was composed of two
262 dimers of mushroom-like structures resembling F_1-ATPase, aligned along the dimer
263 axis (Fig. 5D). Dimers were connected by a bulge structure with a diameter of 5
264 nm. The chain interval was 31 nm, consistent with the corresponding dimension in
265 a 2D image from electron cryotomography (ECT) (23), suggesting that the 3D
266 model obtained reflects the original structure from a cell. The mushroom-like
267 structure with a diameter of 15 nm, consisting of a hexameric ring and a central
268 stalk, was connected to the dimer by two bridge structures with a diameter of 3–6
269 nm. An atomic model of F_1-ATPase catalytic $(\alpha\beta)_3$ from *Bacillus* PS3 (PDB ID
270 6N2Y) (39) was fitted into each hexameric ring of the mushroom-like structure (Fig.
271 5E). The distance between the centers of the fitted $(\alpha\beta)_3$ in Dimer was 12.5 nm,
272 which is consistent with that of Dimer observed by negative-staining EM and HS-
273 AFM (Fig. 3C and H). The fitted model showed that each hexameric ring had two
274 protrusions of 3–6 nm pointing laterally (Fig. 5E). The cross-sections of each
275 mushroom-like structure showed the central stalk length of 5 nm (Fig. 5F). A cavity
276 was observed at the center of the hexameric ring. However, it may be an artifact of
277 the low-resolution map of negative-staining EM, because metal coating tends to
278 emphasize the peripheral part of large particles (40). Next, we compared a
279 reprojection image of the 3D chain map with the 2D averaged image of Dimer from
280 negative-staining EM (Fig. 5G). Two short filaments marked by asterisks in Dimer
281 (Fig. 5G, left) are positioned facing each other in the connecting bulge (Fig. 5G).

282 Previously, ECT of a permeabilized *M. mobile* cell showed a chain structure
283 characterized by repeats of two globules and two types of projections to the cell
284 membrane (Fig. 5H, left) (23). The hexameric ring and the central stalk in the 3D
285 map here correspond to the globule and one type of projection to the cell
286 membrane in the ECT image, respectively, suggesting that the chain is oriented
287 with the central stalk facing the membrane, which is common in F_1-ATPases. At the
288 interface between Dimers, the 3D map here did not include a structure composed
289 of another type of projection and a globule as observed in the ECT image. The
290 subunits corresponding to these structures probably had structural variations or
291 dissociation during the isolation process.
292

293 **Discussion**

294 **Outline of internal structure of gliding machinery.** Previously, sequence
295 analysis suggested that the chain of *M. mobile* gliding machinery evolved from F_1-
296 ATPase (5, 23-26). The present study supports this conclusion by structural data
297 showing that the chain has hexameric rings similar to the F_1-ATPase catalytic $(\alpha\beta)_3$.
298 Integrating available information, we can now describe the outline of the internal
299 structure of *the M. mobile* gliding machinery (Fig. 1A). *M. mobile* cells have 28
300 individual 530 nm long chains, each of which contains 17 Dimer units composed of
301 two F_1-like ATPases and filamentous structures (23). The central stalk of the F_1-like
302 ATPase and another protrusion from the connecting bulge project to the cell

303 membrane.

304 **Unique role of F_1-ATPase related complex.** To date, several complexes are
305 known to be evolutionarily related to F_1-ATPase, all of which are responsible for
306 transporting substances across the membrane (41). However, the motor we
307 identified here most likely plays a role in motility. This case may be reminiscent of
308 dynein, a motor in eukaryotes, which evolved from a widely conserved AAA
309 (ATPases associated with diverse cellular activities)+ protein, in which multiple
310 subunits of ATPases perform functional rotation (42, 43). Sequence analyses have
311 shown that mycoplasma Type 3 ATPase is also related to F_1-ATPase, and its role
312 has been suggested to promote substrate turnover in the MIB-MIP system (33). If
313 Type 3 ATPase provides the force to change the conformation of a hydrolytic
314 enzyme, its role in force generation is common with Type 2, the gliding motor.

315 F_1F_o-ATPases are known to be dimerized through interactions between F_o-
316 domains and are usually arranged in rows along the short axis in the tightly curved
317 cristae ridges of mitochondria (31, 44, 45). The dimer structure found in the present
318 study is not related to this, because the F_1-like domain is dimerized through the
319 filament structure and is linked in the long axis direction. However, some roles may
320 be common in part if the dimerization and chain formation observed in the gliding
321 motor identified in this study stabilizes the membrane structure, as seen in the
322 F_1F_o-ATPase dimer (46). Moreover, dimerization may result in cooperativity in
323 motor functions.

324 **Protein assignment.** The α-subunit homolog MMOB1660 (58.7 kDa) and the β-

325 subunit homolog MMOB1670 (88.4 kDa) likely correspond to the smaller and larger
326 subunits, respectively, of the hexameric ring of an F_1-like ATPase unit, as
327 suggested by the estimated 1:1 molar ratio in Dimer (Fig. 2A, 4C). This means that
328 the hook structure of the larger subunit may be formed by the extra N-terminal
329 region (34.8 kDa) of MMOB1670. Previously, 3D structure modeling based on
330 secondary structure suggested that MMOB1630 is structurally similar to the γ
331 subunit, the principal component of the central stalk of F_1-ATPase (5). In general,
332 the γ subunit of F_1-ATPase is composed of a coiled-coil and a globular domain and
333 penetrates the hexameric ring (47). In the F_1-like ATPase unit and chain 3D model,
334 a stalk structure, suggesting the globular domain of the γ subunit, was found in the
335 center of the hexameric ring (Fig. 4C and 5F), implying that MMOB1630 penetrates
336 the hexameric ring like the γ subunit.
337 Using HS-AFM observations, the peak at approximately 5 nm at the center of the
338 hexameric ring dropped out with time (Fig. 3I). The peak height agrees with the
339 length of the estimated globular domain of MMOB1630 in Chain 3D model (Fig. 3J
340 and 5F), suggesting that the peak is composed of MMOB1630 and was pulled out
341 from the hexameric ring by the scanning cantilever during HS-AFM observation.
342 The pull-out event is thought to be common to that of the F_1-ATPase, in which the γ
343 subunit is removed from the hexameric ring by optical tweezers (48).The
344 filamentous structures around the hexameric ring probably correspond to lateral
345 protrusions in the HS-AFM images and are formed by the remaining proteins,
346 MMOB1620 and MMOB4530 (PGK). These proteins probably play roles in ATPase

347 dimerization, chain formation, and lateral chain interaction (23). MMOB1620 is an
348 unannotated protein specific to the Type 2 ATPase cluster (26, 32). MMOB4530 is
349 annotated as an enzyme that transfers phosphate groups from 1,3-
350 bisphosphoglycerate to ADP in glycolysis to yield ATP and 3-phosphoglycerate
351 (49). In *M. mobile*, ATP is probably provided by glycolysis (50). MMOB4530 may
352 supply ATP efficiently to the gliding motor by its close proximity. Yeast V-ATPase,
353 which belongs to the rotary ATPase family like F_1F_o-ATPase, is also attached by
354 two glycolytic enzymes, 6-phosphofructo-1-kinase and aldolase (51-53). These
355 glycolytic enzymes are involved in the regulation of V-ATPase assembly and
356 activity.

357 Ten proteins have been identified as the components of the internal structure
358 (Fig. 1) (23, 24, 26). In the present study, we identified five proteins as the Dimer
359 components. Other five proteins are likely involved in other parts, for example “bell”
360 at the front part of internal structure (Fig. 1A) and parts of the intact chain structure
361 which were lost in the fractionation (Fig. 5H).

362 **Possible force transmission mechanisms for gliding.** The involvement of an
363 internal ATPase in the gliding mechanism is based on the following five
364 observations from the analysis of the "gliding head” of *M. mobile* protrusions and of
365 the isolated gliding machinery: (a) The affinity for ATP estimated by the saturation
366 extent is comparable in the ATPase activity of the internal structure and the speed
367 of the gliding head (23). (b) Substrate binding and gliding speed of the gliding head
368 are inhibited by azide, as well as the ATPase activity of the internal structure (23).

369 (c) The chain in the internal structure undergoes conformational changes based on
370 ATP hydrolysis (23, 34). (d) Among the 21 proteins identified from the gliding head,
371 only MMOBs 1660 and 1670 could be suggested for ATPase from the amino acid
372 sequences alone (23, 24). (e) Fluorescent protein tagging of components of the
373 internal structure significantly affects the substrate binding of cell and the gliding
374 speed (26).

375 The structure elucidated in the present study allows us to discuss the gliding
376 mechanism in more detail. In F_1-ATPase, the three catalytic sites in the hexameric
377 ring cooperatively hydrolyze ATP, and each catalytic β-subunit undergoes a
378 conformational change that drives the rotation of the central stalk (47). Previously,
379 structural changes linked to ATP hydrolysis were reported: (I) EM studies showed 2
380 nm contraction of Dimer intervals in the isolated chains (23), and (II) HS-AFM
381 studies showed movements of individual Dimers in the cell 9 nm perpendicular to
382 the chain long axis and 2 nm into the cell (34). Considering these observations, we
383 propose two different working models for the force transmission mechanism in
384 gliding (Fig. 6). In the “contraction model” (Fig. 6 i), the force generated by the
385 hexameric ring shortens the chain. The resulting displacement of the projections
386 from Dimer to the cell membrane drives the hook structure of Gli521 like a "lever.”
387 Then, the leg moves with the catch, pull, and release of the SOs. In the “rotation
388 model” (Fig. 6 ii), the force generated by the hexameric ring rotates MMOB1630 in
389 the same way as F_1-ATPase. This rotation is transmitted across the cell membrane
390 to the Gli521. The hook structure converts rotational motion into linear motion of

391 the leg, similar to a crank. Previous studies have reported that *M. mobile* exhibits
392 unitary steps of approximately 70 nm in size at no load (29, 54). In our models,
393 both the rotation and contraction displacements are expected to be a few
394 nanometers. These displacements may be amplified by the large surface structure
395 complex formed by the 100 nm long Gli349 and 120 nm long Gli521, which show
396 dimensions comparable to the step size, acting as a large gear (22). This
397 conjecture could explain how a single leg exerts a force of 1.5 pN, smaller than that
398 of conventional motor proteins such as myosin, dynein, and kinesin.

399 **Evolution of *M. mobile* gliding.** A previous study suggested that Gli349 evolved
400 from a static binding receptor to parasitize the host (16). Considering this, the
401 evolutionary origin of *M. mobile* gliding can now be discussed. F_1F_o-ATPase, which
402 is abundant on the cell membrane, could have been accidentally associated with
403 the binding receptor and turned into a primitive motility system, which may have
404 provided random cell spreading. The system was then refined under survival
405 pressure, because motility might be beneficial to infection and evading the host's
406 immune system. For dimerization and chain formation, PGK was then incorporated
407 into the gliding machinery, because PGK was working in close proximity to F_1F_o-
408 ATPase.

409

410 **Materials and Methods**

411 **Strains and culture conditions.** We used P476R *gli521*, a mutant strain of *M.*
412 *mobile* that can glide normally but binds SOs more tightly than wild-type strains

413 (10, 22, 28). *M. mobile* cells were cultured as described previously (55, 56).

414 **Optical microscopy.** The cultured cells were inserted into a tunnel chamber
415 assembled with two coverslips and double-sided tapes and observed by phase-
416 contrast microscopy using an inverted microscope (IX71; Olympus, Tokyo, Japan)
417 (17, 19). Movement was recorded using a complementary metal-oxide
418 semiconductor (CMOS) camera (DMK33UX174; The Imaging Source, Bremen,
419 Germany). Video was analyzed using the ImageJ software, version 1.53a
420 (http://rsb.info.nih.gov/ij/).

421 **Solubility test.** All procedures for fractionation were performed at 4°C unless
422 otherwise noted and focused protein bands were identified by peptide mass
423 fingerprinting (PMF), as previously reported (24, 57). To investigate the solubility of
424 the chain components, *M. mobile* cells from 60 mL of culture medium were
425 collected by centrifugation at 14000 × *g* for 20 min and washed twice with PBS
426 consisting of 8.1 mM Na_2HPO_4, 1.5 mM KH_2PO_4, pH 7.3, 2.7 mM KCl and 137 mM
427 NaCl. Cells were resuspended in PBS to a 12-fold higher concentration than the
428 culture and sonicated for 1 min at 24–27°C to be dispersed in microtubes using an
429 ultrasonic generator (2510 J-MT; BRANSON, Kanagawa, Japan). The cells were
430 then treated with Triton solution (1% Triton X-100, 0.1 mg/mL DNase, 5 mM $MgCl_2$,
431 and 1 mM phenylmethylsulfonyl fluoride in PBS) in a total volume of 10 mL. After
432 gentle shaking for 1 h, the suspensions were centrifuged at 20000 × *g* for 20 min,
433 and pellets were collected and washed once with suspension buffer (PBS including
434 5 mM $MgCl_2$). This fraction is Pellet-1. Pellet-1 was then resuspended separately in

435 suspension buffer adjusted to contain different concentrations of NaCl (0, 50, 137,
436 200, and 400 mM) by pipetting several times. After treatment for 8 h, suspensions
437 were centrifuged at 20000 × *g* for 20 min, and supernatants and pellets collected
438 for SDS-PAGE analysis.

439 **Preparation of fractions.** For isolation of Dimer, Pellet-1 from 1.2-liter culture
440 was resuspended in 5 mL suspension buffer by pipetting up and down and allowed
441 to dissolve for 8 h. The soluble fraction was collected by centrifugation at 20000 ×
442 *g* for 20 min and loaded onto a HiLoad 16/600 Superdex 200 column (Cytiva,
443 Tokyo, Japan) equilibrated with 1 mM $MgCl_2$ in PBS at a flow rate of 0.8 mL/min.
444 The fractions were analyzed by SDS-PAGE and CBB staining.

445 For isolation of Monomer, Pellet-1 from 1.2-liter culture was suspended by 5
446 mL Tris buffer consisting of 20 mM Tris-HCl (pH 7.5), 250 mM NaCl, 1 mM
447 phenylmethylsulfonyl fluoride, and 1 mM $MgCl_2$ with pipetting and allowed to
448 dissolve for 8 h. The soluble fraction was collected by centrifugation at 20000 × *g*
449 for 20 min and mixed with 1.5% (w/v) sodium cholate. After 7 h of incubation, the
450 complexes were loaded onto a Sephacryl S-400 HR column (Cytiva) equilibrated
451 with 0.7% sodium cholate, 20 mM Tris-HCl (pH 7.5), 250 mM NaCl, and 1 mM
452 $MgCl_2$ at a flow rate of 0.5 mL/min. The fractions were analyzed by SDS-PAGE and
453 CBB- and reverse-staining (58, 59). The fraction of the complex composed of
454 MMOBs 1670, 1660, and 1630 was collected. Samples were concentrated using
455 an Amicon Ultra 100 K spin filter (Merck KGaA, Darmstadt, Germany), if necessary.

456 For isolation of Chain, Pellet-1 from 15 mL culture was resuspended in 60 μL

457 suspension buffer. The suspension was then gently mixed with an equal volume in
458 a suspension buffer adjusted to contain 637 mM NaCl. Chain was recovered as the
459 supernatant by centrifugation at 5000 × *g* for 5 min.

460 **Analytical gel filtration.** Dimer solution was loaded onto a Sephacryl S-400
461 HR column equilibrated with gel filtration buffer containing 20 mM Tris-HCl (pH
462 7.5), 200 mM NaCl and 1 mM $MgCl_2$ at a flow rate of 0.5 mL/min at 4°C.
463 Thyroglobulin (669 kDa; Gel Filtration Calibration Kits; Cytiva) was dissolved in gel
464 filtration buffer and loaded onto the column as a size standard at a flow rate of 0.5
465 mL/min. The stoichiometry of protein complexes was estimated by densitometry of
466 SDS-PAGE gels stained with CBB, using a scanner (GT-9800F; Epson, Nagano,
467 Japan) and ImageJ (9).

468 **BN-PAGE and in-gel ATPase activity assays** BN-PAGE was performed
469 according to the user manual of the Native PAGE Novex Bis-Tris Gel System
470 (Thermo Fisher Scientific, Waltham, MA). For BN-PAGE of sodium cholate treated
471 Dimer, SC treated, Dimer fraction was mixed with sodium cholate (1.5%) and
472 incubated at 4°C for 9 h. When this sample was mixed with a sample buffer,
473 NativePAGE™ 5% (w/v) G-250 sample additive was also added at 0.5% (w/v) to
474 prevent protein aggregation. Thyroglobulin was dissolved in water and used as a
475 negative control for the In-gel ATPase activity assay. For the In-gel ATPase activity
476 assay (60, 61), native gels were incubated with gentle shaking for 8h at 24–27°C in
477 activity buffer containing 270 mM glycine, 35 mM Tris (pH 8.4), 4 mM ATP, 14 mM
478 $MgSO_4$, and 0.2% (w/v) $Pb(NO_3)_2$. The gels were rinsed once with water and

479 images were taken using ImageQuant LAS 4000 mini (Cytiva). White precipitates
480 were then dissolved by gentle shaking for 8 h at 24–27°C with 50% (v/v) methanol
481 and 10% (v/v) acetic acid in water. The gels were restained with 0.025% (w/v) CBB
482 G-250 and 10% acetic acid in water for 80 min at 24–27°C with gentle shaking and
483 destained with 10% (v/v) ethanol and 10% acetic acid in water for 180 min at 24–
484 27°C with gentle shaking. The gels were rinsed once with water and images were
485 taken using ImageQuant LAS 4000 mini.

486 **Phosphate-release assay** Dimer solution was dialyzed for 8 h using 20 mM
487 Tris-HCl (pH 7.5), 150 mM NaCl, and 2 mM $MgCl_2$. ATPase activity was assayed
488 by a continuous spectrophotometric method using a 2-amino-6-mercapto-7-
489 methylpurine ribonucleoside–purine nucleoside phosphorylase reaction to detect
490 released inorganic phosphate (EnzChek kit; Thermo Fisher Scientific) (62). The
491 reaction mixture was as follows: 15.7 nM Dimer, 20 mM Tris-HCl (pH 7.5), 150 mM
492 NaCl, 2 mM $MgCl_2$ and 0.01–1 mM ATP in a total volume of 0.2 mL at 25°C.
493 Sodium azide was added to 15.4 mM final concentration when the reaction was
494 started. The protein amount of the MMOB1670 comprising F_1-ATPase β-subunit
495 paralogs was estimated using densitometric of SDS-PAGE.

496 **Negative-staining EM and image processing.** Dimer solution was placed on
497 a glow-discharged (PIB-10; VACUUM DEVICE, Ibaraki, Japan) carbon-coated grid
498 (F-400; Nisshin EM Co., Tokyo, Japan) and incubated for 1 min at 24–27°C. The
499 solution was then removed, and the grid was stained with 2% uranyl acetate (w/v)
500 for 30 s. The stain was then removed, and the grid was air-dried. To observe

501 Monomer and Chain, the grids were washed with water after 1 min of incubation
502 and then treated as described for Dimer solution. Samples were observed using a
503 transmission EM (JEM1010, JEOL) at 80 kV, equipped with a FastScan-F214 (T)
504 charge-coupled-device (CCD) camera (TVIPS, Gauting, Germany), and images
505 were captured at 2.58 Å/pix.

506 The contrast transfer function parameters for electron micrographs were
507 estimated using Gctf (63). Further image processing was performed using RELION
508 3.0 (36). A total of 2148 particles for Dimer and 11687 particles for Monomer were
509 automatically selected with box sizes of 180 × 180 and 100 × 100 pixels using
510 reference-based auto-picking, respectively. These particle images were binned to
511 5.16 Å/pix. For Dimer, the particle images were 2D-classified into 100 classes. For
512 Monomer, particle images were 2D-classified in four rounds, and the selected 7381
513 particles were re-extracted with the pixel size returned to the unbinned image and
514 then 2D-classified into 50 classes.

515 For reconstruction of the 3D chain structure, 2127 particles were manually
516 selected for chains with a box size of 276 × 276 pixels with ~50% overlap. These
517 particle images were binned to 5.16 Å/pix. Particle images were 2D-classified in
518 two rounds, and the selected 1709 particles were used to reconstruct the initial
519 model with a final resolution limit of 50 Å. The initial model and selected particles
520 were used to perform 3D refinement. Reprojection images were produced from the
521 3D map using the relion_project command in RELION. The 3D map was visualized
522 using UCSF Chimera 1.14 (64). Atomic models of F_1-ATPase catalytic $(\alpha\beta)_3$ from *B.*

523 *subtilis* (PDB ID 6N2Y) (39) were fitted into the 3D map using command of “Fit in
524 map” in UCSF Chimera.

525 **HS-AFM.** Imaging was performed with a laboratory-built tapping mode HS-
526 AFM (65, 66), using small cantilevers (BLAC10DS-A2, Olympus; resonant
527 frequency, ~0.5 MHz in water; quality factor, ~1.5 in water; spring constant, ~0.1
528 N/m). The cantilever’s free-oscillation peak-to-peak amplitude (A_0) and set-point
529 amplitude were set at ~2.5 nm and ~0.8 × A_0, respectively. The probe tip was
530 grown on the original tip end of a cantilever through electron beam deposition and
531 further sharpened using a radio frequency plasma etcher (PE-2000, South Bay
532 Technology, Redondo Beach, CA) under an argon gas atmosphere (typically at 180
533 mTorr and 15 W for 3 min). The sample was deposited on a freshly cleaved mica
534 disc glued to a glass stage beforehand. After 3.5 min, the stage surface was
535 immersed in a liquid cell containing an observation buffer [20 mM Tris-HCl (pH 7.5),
536 50 mM KCl, 2 mM $MgCl_2$]. Imaging was performed at 24–27°C. AFM images were
537 processed using a low-pass filter to remove spike noise and make the *xy*-plane flat
538 and analyzed using Kodec software (version 4.4.7.39) (67). Surface profiles and
539 smoothing were performed using ImageJ software.
540

541 ## Acknowledgments

542 We thank Toshiaki Arata, Ikuko Fujiwara, Kohei Kobayashi, and Hiroki Sato at the
543 Graduate School of Science, Osaka City University, and Takayuki Uchihashi at the

544 Department of Physics and Structural Biology Research Center, Nagoya University,
545 for helpful discussions. We also thank Aya Takamori at the Graduate School of
546 Science, Osaka City University, for performing MALDI-TOF MASS spectrometry.
547 TT learned RELION software in an instruction course on 20180927–28 provided by
548 the Cyclic Innovation for Clinical Empowerment (CiCLE) from AMED.
549 This work was supported by a Grant-in-Aid for Scientific Research on the
550 Innovative Area "Harmonized Supramolecular Motility Machinery and Its Diversity"
551 (MEXT KAKENHI Grant Number JP24117002), by a Grants-in-Aid for Scientific
552 Research (B) and (A) (MEXT KAKENHI Grant Numbers JP24390107,
553 JP17H01544), by JST CREST Grant Number JPMJCR19S5, Japan, by the Osaka
554 City University (OCU) Strategic Research Grant 2018 for top priority researches
555 and by a Grant-in-aid of the FUGAKU TRUST FOR MEDICINAL RESEARCH to
556 MM, and JSPS KAKENHI (Grant Number JP25000013), the Platform Project for
557 Supporting Drug Discovery and Life Science Research (BINDS) from AMED (Grant
558 Number JP19am0101117 and support number 1282), CiCLE (Grant Number
559 JP17pc0101020), and JEOL YOKOGUSHI Research Alliance Laboratories of
560 Osaka University to KN.
561

562 ## Figure Legends

563 **FIG 1. Gliding machinery of *Mycoplasma mobile*.** (A) Schematic illustration of
564 gliding machinery based on the present study. In the whole cell shown in upper
565 illustration, the internal structure and legs are colored gray and red, respectively.

566 The actual cell has about 28 chains, each consisting of 17 particles, although a
567 more limited number is illustrated here. In this paper we refer to particle and F_1-like
568 ATPase unit as the “Dimer” and the “Monomer”, respectively. A single unit of the
569 surface structure and a chain of the internal structure are magnified in the lower
570 illustration. (B) ORFs for the internal structure. The components of the internal
571 structure are colored gray. Type 2 ATPase operon is at the top. Dimer components
572 revealed in the present study are marked by colored boxes, corresponding to the
573 colored components of the lower illustration in panel A.
574
575 **FIG 2. Protein profile and characterization of three fractions.** (A) Protein profile
576 of each fraction. Dimer, Monomer, and Chain fractions were subjected to SDS-
577 12.5% PAGE gel and stained with CBB. The bands marked by black triangles were
578 identified by peptide mass fingerprinting (PMF). The intensity of band marked by an
579 asterisk is reduced in Monomer fraction. Molecular masses are shown on the left.
580 (B) Gel filtration assay of unit complex fraction using Sephacryl S-400 HR column.
581 The peak positions of unit complex (Dimer) and thyroglobulin (669 kDa) are
582 marked by orange and purple triangles. (C) BN-PAGE (left) and In-gel ATPase
583 activity assay (right). Dimer, Dimer treated with 1.5% sodium cholate (SC treated),
584 and thyroglobulin, which has no ATPase activity, were subjected to 3 to 12%
585 gradient BN-PAGE. The bands of Dimer and Monomer after sodium cholate
586 treatment are marked by closed and open triangles. White lead phosphate bands,
587 indicating ATPase activity appeared in the right panel. Molecular masses are

588 shown on the left. (D) Phosphate release assay of Dimer under various ATP
589 concentrations with and without sodium azide. The ATPase activities under 0- and
590 15.4-mM sodium azide are marked by red and green filled circles, respectively (*n* =
591 3). These data were fitted by the Michaelis-Menten equation as solid lines.
592
593 **FIG 3. Negative-staining EM and HS-AFM of Dimer.** (A) Electron micrograph of
594 negatively stained particles in unit complex fraction. (B) Images of individual
595 particles. (C) Representative 2D averaged image. A mirror image is shown to
596 match the orientation of the hexameric ring observed by HS-AFM. (D) Illustration
597 based on the averaged image in panel C. Filamentous structures are marked by
598 asterisks at an end. The double-headed arrow shows the distance between the
599 centers of the hexamers. (E) Two patterns of HS-AFM images. A Dimer was
600 scanned at 56 × 56 pixels in an area of 70 × 70 nm^2 with a scanning rate of 100 ms
601 per frame. Illustrations for patterns I and II (left side) were depicted based on 3D
602 chain model shown in Fig. 5. Observation directions are indicated by arrows.
603 Protrusions are marked by blue triangles. Images of patterns I and II are shown in
604 green and purple frames, respectively. (F) Averaged images for patterns I (green
605 frame) and II (purple frame). Dimer was scanned at 50 × 50 pixels in an area of 40
606 × 40 nm^2 with a scanning rate of 100 ms per frame. The images were produced by
607 averaging three successive video frames. (G) HS-AFM slice image showing two
608 hexameric rings (upper) and averaged EM image (lower). Upper: The red broken
609 boxed area in panel F was sliced for the height 9.8–11.3 nm from the substrate

surface, processed for smoothing, and magnified. The angle alignments of two hexamers are schematically shown in the left upper. Lower: The central part of panel C was excised and aligned to compare with the upper panel. Subunits of the hexamer are marked by red circles. (H) Surface profiles along the lines in pattern I (green) and II (purple). The upper and lower images in panel F were each profiled at the green and purple lines passing the globule centers. The dimples and the peaks are marked by open and black triangles, respectively. The slice height in panel G is shown by broken lines. (I) Shedding process of the peaks of pattern II particle shown in panel E. The peaks are marked by red triangles. (J) Surface profile showing the disappeared peaks. The images in panel I were each profiled at the blue, pink, and light blue lines passing the globule centers. The peaks are marked by black triangles. The double-headed arrows show the peak heights. (K) HS-AFM image of Dimer with seven lateral protrusions. Dimer was scanned at 120 × 120 pixels in an area of 120 × 120 nm^2 with a scanning rate of 500 ms per frame. Lateral protrusions are indicated by blue triangles. (L) Fluctuations of the protrusions of the particle shown in panel K. The images were sliced for the height 0–7.0 nm from the substrate surface. The moving directions are indicated by arrows. In all HS-AFM images, the color bar on the right shows the range of image heights.

FIG 4. Negative staining EM of Monomer fraction. (A) Electron micrograph of negatively stained ATPase in Monomer fraction. (B) Images of individual particles.

632 (C) Representative 2D averaged images (upper) and depictions of their structures
633 (lower). Upper: Hook structures in the hexameric ring and the stalks are marked by
634 green and orange triangles, respectively. Lower: The hexameric part, hook
635 structures and the stalk are colored rose, green and orange, respectively.
636
637 **FIG 5. Chain structure.** (A) Electron micrograph of negatively stained Chain. The
638 chain structures are marked by blue lines. (B) Magnified chain images. (C)
639 Representative 2D averaged images. (D) Three-dimensional reconstruction of
640 Chain containing two F_1-like ATPase dimers. The 3D map is visualized at a density
641 threshold (contour level = 0.026). The central stalks are marked by open triangles.
642 (E) Superposition of the atomic model of *Bacillus* F_1-ATPase catalytic $(\alpha\beta)_3$ (PDB
643 ID 6N2Y) (39) onto the 3D chain structure. The α and β subunits are colored
644 salmon and turquoise, respectively. The central stalk and protrusions from
645 hexameric rings are marked by open and black triangles, respectively. (F) Cross
646 section of mushroom-like structures. Central stalks are marked by broken circles.
647 The double-headed arrow shows the length of the protrusion. Corresponding
648 mushroom-like structures are marked (a)–(d) in panel E. (G) Comparison between
649 Dimer image from Fig. 3C (left) and the Chain reprojection (middle). The
650 reprojected image is viewed from the angle used for the right image of panel D.
651 Short filaments corresponding to the position of the connecting bulge are marked
652 by asterisks. A depiction of Chain model based on the comparison (right). (H)
653 Comparison between the averaged chain image from ECT (left) and the chain

654 reprojection (middle). Left: The averaged chain image was modified from the whole
655 cell ECT image in the previous study (23). Middle: Chain was reprojected from an
656 angle close to the middle image in panel D. Inner sides and membrane relative to
657 the chain are marked by i and m, respectively. The protrusion from the globule
658 corresponding to the central stalk from the hexameric ring, one from the connecting
659 bulge and the globule attached to the connecting bulge are marked by orange, light
660 blue and green triangles, respectively. The areas of image densities that were
661 visualized only in the ECT image are marked by broken lines. Right: An illustration
662 depicts a chain model based on the comparison.
663
664 **FIG 6. Working models for force transmission mechanism.** The gliding
665 direction is indicated by a red arrow. The regions marked in gray were visualized
666 only in the ECT image. The crank protein Gli521 and the leg protein Gli349 are
667 colored green and red, respectively. (i) Contraction model: The force generated by
668 the hexameric ring displaces Dimer along the gliding direction. The displacements
669 are transmitted through the membrane to Gli521. (ii) Rotation model: The force
670 generated by the hexameric ring rotates the central stalk in a mechanism similar to
671 that of F_1-ATPase. The rotational motion is transmitted across the membrane to
672 Gli521.The generation and transmission of forces are presented by black arrows
673 for both models.
674
675 **FIG S1 Gliding of *M. mobile* cells.** Optical microscopy of cells (left) and

676 trajectories of gliding cells (right). All cells are gliding in the direction of tapered end
677 as indicated by a black arrow. For trajectories, video frames of every 0.2 s were
678 colored differently from red to blue, and stacked for 4 s.
679
680 **FIG S2 Isolation procedure for three fractions.** Each fraction was obtained from
681 Pellet-1 fraction. The adjusted concentrations of NaCl in the solution are indicated
682 in parentheses. Supernatant is abbreviated as “Sup”. See Materials and Methods
683 for details.
684
685 **FIG S3 Isolation profile of Dimer (unit complex) and Monomer fractions.** (A)
686 Solubility of the chain components. Pellet-1 fraction was treated with buffers
687 containing the specified concentrations of NaCl and centrifuged. Pellet-1 fraction,
688 the supernatants (S) and the pellets (P) were analyzed by SDS-12.5% PAGE. See
689 Materials and Methods for details. (B) Isolation of Dimer (unit complex). The
690 fractions of each step were subjected to SDS-12.5% PAGE gel and stained with
691 CBB. Lane 1, lysate of *M. mobile* cells; lane 2, Triton-soluble fraction; lane 3,
692 Triton-insoluble (Pellet-1) fraction; lane 4, supernatant after incubation in
693 suspension buffer containing 137 mM NaCl; lane 5, peak fraction of Superdex 200
694 gel filtration chromatography. The bands of Dimer components are marked by
695 black triangles. (C) Gel filtration profile in Monomer isolation using a Sephacryl S-
696 400 HR column. The small peak is marked by a green triangle. (D) The F1–F13
697 fractions in the gel filtration indicated by the green line in panel C were subjected to

698 SDS-12.5% PAGE and stained with CBB. F6, which corresponds to the small peak
699 in the gel filtration, was used for further analyses as Monomer fraction. Bands of
700 Dimer components are marked by black triangles. For panels (A, B, D), Focused
701 proteins were identified by PMF, and molecular masses are shown on the left.
702
703 **FIG S4 Two-dimensional averaged images of Dimer obtained by negative-**
704 **staining EM.** Four classes of clear particle images from 20 classes are
705 represented. These images have common features as represented long and short
706 protrusions marked by light blue and orange triangles, respectively. As mentioned
707 in Fig. 3C, the images were mirrored to uniform handedness.
708
709 **FIG S5 Two-dimensional averaged images of globular complex in Monomer**
710 **fraction.** Fifteen classes of clear particle images from 50 classes are represented.
711
712 **FIG S6 Reprojection images of Chain.** Two-dimensional averaged images
713 (upper) and the corresponding reprojection images (lower) calculated from the 3D
714 map of Chain are compared.
715
716 **Movie S1 HS-AFM movie showing pattern I particles** The particles were
717 scanned at 10 fps. The scanning field was 70 × 70 nm^2 with 56 × 56 pixels. The
718 video was played at 10 fps.
719

720 **Movie S2 HS-AFM movie showing pattern II particles** The particles were
721 scanned at 10 fps. The scanning field was 70 × 70 nm^2 with 56 × 56 pixels. The
722 video was played at 10 fps.
723
724 **Movie S3 HS-AFM movie showing the shedding process of the peaks.** The
725 particles were scanned at 10 fps. The scanning field was 70 × 70 nm^2 with 56 × 56
726 pixels. The video was played at 10 fps. The peaks are indicated by the red
727 triangles.
728
729 **Movie S4 HS-AFM movie showing fluctuations in protrusions.** The particles
730 were scanned at 2 fps. The scanning field was 120 × 120 nm^2 with 120 × 120
731 pixels. The video was played at 1 fps. The protrusions are indicated by the red
732 triangles.
733

734 References

735 1. Razin S, Hayflick L. 2010. Highlights of mycoplasma research--an historical
736 perspective. Biologicals 38:183-90.
737 2. Grosjean H, Breton M, Sirand-Pugnet P, Tardy F, Thiaucourt F, Citti C, Barre
738 A, Yoshizawa S, Fourmy D, de Crecy-Lagard V, Blanchard A. 2014.
739 Predicting the minimal translation apparatus: lessons from the reductive
740 evolution of mollicutes. PLoS Genet 10:e1004363.
741 3. Miyata M, Robinson RC, Uyeda TQP, Fukumori Y, Fukushima SI, Haruta S,

742 Homma M, Inaba K, Ito M, Kaito C, Kato K, Kenri T, Kinosita Y, Kojima S,
743 Minamino T, Mori H, Nakamura S, Nakane D, Nakayama K, Nishiyama M,
744 Shibata S, Shimabukuro K, Tamakoshi M, Taoka A, Tashiro Y, Tulum I, Wada
745 H, Wakabayashi KI. 2020. Tree of motility - A proposed history of motility
746 systems in the tree of life. Genes Cells 25:6-21.
747 4. Miyata M. 2010. Unique centipede mechanism of *Mycoplasma* gliding. Annu
748 Rev Microbiol 64:519-37.
749 5. Miyata M, Hamaguchi T. 2016. Prospects for the gliding mechanism of
750 *Mycoplasma mobile*. Curr Opin Microbiol 29:15-21.
751 6. Miyata M, Hamaguchi T. 2016. Integrated information and prospects for
752 gliding mechanism of the pathogenic bacterium *Mycoplasma pneumoniae*.
753 Front Microbiol 7:960.
754 7. Uenoyama A, Kusumoto A, Miyata M. 2004. Identification of a 349-kilodalton
755 protein (Gli349) responsible for cytadherence and glass binding during
756 gliding of *Mycoplasma mobile*. J Bacteriol 186:1537-45.
757 8. Seto S, Uenoyama A, Miyata M. 2005. Identification of a 521-kilodalton
758 protein (Gli521) involved in force generation or force transmission for
759 *Mycoplasma mobile* gliding. J Bacteriol 187:3502-10.
760 9. Uenoyama A, Miyata M. 2005. Identification of a 123-kilodalton protein
761 (Gli123) involved in machinery for gliding motility of *Mycoplasma mobile*. J
762 Bacteriol 187:5578-84.
763 10. Uenoyama A, Seto S, Nakane D, Miyata M. 2009. Regions on Gli349 and

764 Gli521 protein molecules directly involved in movements of *Mycoplasma*
765 *mobile* gliding machinery, suggested by use of inhibitory antibodies and
766 mutants. J Bacteriol 191:1982-5.
767 11. Kusumoto A, Seto S, Jaffe JD, Miyata M. 2004. Cell surface differentiation of
768 *Mycoplasma mobile* visualized by surface protein localization. Microbiology
769 150:4001-8.
770 12. Miyata M, Petersen JD. 2004. Spike structure at the interface between
771 gliding *Mycoplasma mobile* cells and glass surfaces visualized by rapid-
772 freeze-and-fracture electron microscopy. J Bacteriol 186:4382-6.
773 13. Adan-Kubo J, Uenoyama A, Arata T, Miyata M. 2006. Morphology of isolated
774 Gli349, a leg protein responsible for *Mycoplasma mobile* gliding via glass
775 binding, revealed by rotary shadowing electron microscopy. J Bacteriol
776 188:2821-8.
777 14. Lesoil C, Nonaka T, Sekiguchi H, Osada T, Miyata M, Afrin R, Ikai A. 2010.
778 Molecular shape and binding force of *Mycoplasma mobile*'s leg protein
779 Gli349 revealed by an AFM study. Biochem Biophys Res Commun
780 391:1312-7.
781 15. Metsugi S, Uenoyama A, Adan-Kubo J, Miyata M, Yura K, Kono H, Go N.
782 2005. Sequence analysis of the gliding protein Gli349 in *Mycoplasma*
783 *mobile*. Biophysics (Nagoya-shi) 1:33-43.
784 16. Hamaguchi T, Kawakami M, Furukawa H, Miyata M. 2019. Identification of
785 novel protein domain for sialyloligosaccharide binding essential to

786 *Mycoplasma mobile* gliding. FEMS Microbiol Lett 366:fnz016.
787 17. Morio H, Kasai T, Miyata M. 2016. Gliding direction of *Mycoplasma mobile*. J
788 Bacteriol 198:283-90.
789 18. Kasai T, Hamaguchi T, Miyata M. 2015. Gliding motility of *Mycoplasma*
790 *mobile* on uniform oligosaccharides. J Bacteriol 197:2952-7.
791 19. Kasai T, Nakane D, Ishida H, Ando H, Kiso M, Miyata M. 2013. Role of
792 binding in *Mycoplasma mobile* and *Mycoplasma pneumoniae* gliding
793 analyzed through inhibition by synthesized sialylated compounds. J
794 Bacteriol 195:429-35.
795 20. Nagai R, Miyata M. 2006. Gliding motility of *Mycoplasma mobile* can occur
796 by repeated binding to *N*-acetylneuraminyllactose (sialyllactose) fixed on
797 solid surfaces. J Bacteriol 188:6469-75.
798 21. Chen J, Neu J, Miyata M, Oster G. 2009. Motor-substrate interactions in
799 *Mycoplasma* motility explains non-Arrhenius temperature dependence.
800 Biophys J 97:2930-8.
801 22. Mizutani M, Tulum I, Kinosita Y, Nishizaka T, Miyata M. 2018. Detailed
802 analyses of stall force generation in *Mycoplasma mobile* gliding. Biophys J
803 114:1411-1419.
804 23. Nishikawa M, Nakane D, Toyonaga T, Kawamoto A, Kato T, Namba K,
805 Miyata M. 2019. Refined mechanism of *Mycoplasma mobile* gliding based
806 on structure, ATPase activity, and sialic acid binding of machinery. mBio
807 10:e02846-19.

808 24. Nakane D, Miyata M. 2007. Cytoskeletal "jellyfish" structure of *Mycoplasma*
809 *mobile*. Proc Natl Acad Sci U S A 104:19518-23.
810 25. Tulum I, Yabe M, Uenoyama A, Miyata M. 2014. Localization of P42 and F_1-
811 ATPase alpha-subunit homolog of the gliding machinery in *Mycoplasma*
812 *mobile* revealed by newly developed gene manipulation and fluorescent
813 protein tagging. J Bacteriol 196:1815-24.
814 26. Tulum I, Kimura K, Miyata M. 2020. Identification and sequence analyses of
815 the gliding machinery proteins from *Mycoplasma mobile*. Sci Rep 10:3792.
816 27. Walker JE, Saraste M, Runswick MJ, Gay NJ. 1982. Distantly related
817 sequences in the alpha- and beta-subunits of ATP synthase, myosin,
818 kinases and other ATP-requiring enzymes and a common nucleotide binding
819 fold. Embo j 1:945-51.
820 28. Uenoyama A, Miyata M. 2005. Gliding ghosts of *Mycoplasma mobile*. Proc
821 Natl Acad Sci USA 102:12754-8.
822 29. Kinosita Y, Nakane D, Sugawa M, Masaike T, Mizutani K, Miyata M,
823 Nishizaka T. 2014. Unitary step of gliding machinery in Mycoplasma mobile.
824 Proc Natl Acad Sci U S A 111:8601-6.
825 30. Abrahams JP, Leslie AG, Lutter R, Walker JE. 1994. Structure at 2.8 A
826 resolution of F1-ATPase from bovine heart mitochondria. Nature 370:621-8.
827 31. Kühlbrandt W. 2019. Structure and Mechanisms of F-Type ATP Synthases.
828 Annu Rev Biochem 88:515-549.
829 32. Beven L, Charenton C, Dautant A, Bouyssou G, Labroussaa F, Skollermo A,

830 Persson A, Blanchard A, Sirand-Pugnet P. 2012. Specific evolution of F_1-like
831 ATPases in mycoplasmas. PLoS One 7:e38793.
832 33. Nottelet P, Bataille L, Gourgues G, Anger R, Lartigue C, Sirand-Pugnet P,
833 Marza E, Fronzes R, Arfi Y. 2021. The mycoplasma surface proteins MIB
834 and MIP promote the dissociation of the antibody-antigen interaction. Sci
835 Adv 7.
836 34. Kobayashi K, Kodera N, Kasai T, Tahara YO, Toyonaga T, Mizutani M,
837 Fujiwara I, Ando T, Miyata M. 2021. Movements of *Mycoplasma mobile*
838 gliding machinery detected by high-speed atomic force microscopy. mBio in
839 press:mBio00040-21.
840 35. Bowler MW, Montgomery MG, Leslie AG, Walker JE. 2006. How azide
841 inhibits ATP hydrolysis by the F-ATPases. Proc Natl Acad Sci U S A
842 103:8646-9.
843 36. Zivanov J, Nakane T, Forsberg BO, Kimanius D, Hagen WJ, Lindahl E,
844 Scheres SH. 2018. New tools for automated high-resolution cryo-EM
845 structure determination in RELION-3. eLife 7:e42166.
846 37. Ando T. 2018. High-speed atomic force microscopy and its future prospects.
847 Biophys Rev 10:285-292.
848 38. Uchihashi T, Iino R, Ando T, Noji H. 2011. High-speed atomic force
849 microscopy reveals rotary catalysis of rotorless F_1-ATPase. Science
850 333:755-8.
851 39. Guo H, Suzuki T, Rubinstein JL. 2019. Structure of a bacterial ATP synthase.

852 eLife 8:e43128.
853 40. Cheng Y, Wolf E, Larvie M, Zak O, Aisen P, Grigorieff N, Harrison SC, Walz
854 T. 2006. Single particle reconstructions of the transferrin-transferrin receptor
855 complex obtained with different specimen preparation techniques. J Mol Biol
856 355:1048-65.
857 41. Dibrova DV, Konovalov KA, Perekhvatov VV, Skulachev KV, Mulkidjanian
858 AY. 2017. COGcollator: a web server for analysis of distant relationships
859 between homologous protein families. Biol Direct 12:29.
860 42. Neuwald AF, Aravind L, Spouge JL, Koonin EV. 1999. AAA+: A class of
861 chaperone-like ATPases associated with the assembly, operation, and
862 disassembly of protein complexes. Genome Res 9:27-43.
863 43. Snider J, Thibault G, Houry WA. 2008. The AAA+ superfamily of functionally
864 diverse proteins. Genome Biol 9:216.
865 44. Minauro-Sanmiguel F, Wilkens S, García JJ. 2005. Structure of dimeric
866 mitochondrial ATP synthase: novel F0 bridging features and the structural
867 basis of mitochondrial cristae biogenesis. Proc Natl Acad Sci U S A
868 102:12356-8.
869 45. Allegretti M, Klusch N, Mills DJ, Vonck J, Kühlbrandt W, Davies KM. 2015.
870 Horizontal membrane-intrinsic α-helices in the stator a-subunit of an F-type
871 ATP synthase. Nature 521:237-40.
872 46. Blum TB, Hahn A, Meier T, Davies KM, Kühlbrandt W. 2019. Dimers of
873 mitochondrial ATP synthase induce membrane curvature and self-assemble

874 into rows. Proc Natl Acad Sci U S A 116:4250-4255.
875 47. Noji H, Ueno H, McMillan DGG. 2017. Catalytic robustness and torque
876 generation of the F_1-ATPase. Biophys Rev 9:103-118.
877 48. Naito TM, Masaike T, Nakane D, Sugawa M, Okada KA, Nishizaka T. 2019.
878 Single-molecule pull-out manipulation of the shaft of the rotary motor F_1-
879 ATPase. Sci Rep 9:7451.
880 49. Watson HC, Walker NP, Shaw PJ, Bryant TN, Wendell PL, Fothergill LA,
881 Perkins RE, Conroy SC, Dobson MJ, Tuite MF. 1982. Sequence and
882 structure of yeast phosphoglycerate kinase. Embo j 1:1635-40.
883 50. Jaffe JD, Stange-Thomann N, Smith C, DeCaprio D, Fisher S, Butler J,
884 Calvo S, Elkins T, FitzGerald MG, Hafez N, Kodira CD, Major J, Wang S,
885 Wilkinson J, Nicol R, Nusbaum C, Birren B, Berg HC, Church GM. 2004.
886 The complete genome and proteome of *Mycoplasma mobile*. Genome Res
887 14:1447-61.
888 51. Lu M, Holliday LS, Zhang L, Dunn WA, Jr., Gluck SL. 2001. Interaction
889 between aldolase and vacuolar H^+-ATPase: evidence for direct coupling of
890 glycolysis to the ATP-hydrolyzing proton pump. J Biol Chem 276:30407-13.
891 52. Lu M, Ammar D, Ives H, Albrecht F, Gluck SL. 2007. Physical interaction
892 between aldolase and vacuolar H^+-ATPase is essential for the assembly and
893 activity of the proton pump. J Biol Chem 282:24495-503.
894 53. Chan CY, Dominguez D, Parra KJ. 2016. Regulation of Vacuolar H^+-ATPase
895 (V-ATPase) Reassembly by Glycolysis Flow in 6-Phosphofructo-1-kinase

896 (PFK-1)-deficient Yeast Cells. J Biol Chem 291:15820-9.
897 54. Kinosita Y, Miyata M, Nishizaka T. 2018. Linear motor driven-rotary motion of
898 a membrane-permeabilized ghost in *Mycoplasma mobile*. Sci Rep 8:11513.
899 55. Miyata M, Yamamoto H, Shimizu T, Uenoyama A, Citti C, Rosengarten R.
900 2000. Gliding mutants of *Mycoplasma mobile*: relationships between motility
901 and cell morphology, cell adhesion and microcolony formation. Microbiology
902 146:1311-20.
903 56. Aluotto BB, Wittler RG, Williams CO, Faber JE. 1970. Standardized
904 bacteriologic techniques for the characterization of *Mycoplasma* species. Int
905 J Syst Bacteriol 20:35-58.
906 57. Kawakita Y, Kinoshita M, Furukawa Y, Tulum I, Tahara YO, Katayama E,
907 Namba K, Miyata M. 2016. Structural study of MPN387, an essential protein
908 for gliding motility of a human-pathogenic bacterium, *Mycoplasma*
909 *pneumoniae*. J Bacteriol 198:2352-9.
910 58. Lee C, Levin A, Branton D. 1987. Copper staining: a five-minute protein
911 stain for sodium dodecyl sulfate-polyacrylamide gels. Anal Biochem
912 166:308-12.
913 59. Dzandu JK, Johnson JF, Wise GE. 1988. Sodium dodecyl sulfate-gel
914 electrophoresis: staining of polypeptides using heavy metal salts. Anal
915 Biochem 174:157-67.
916 60. Zerbetto E, Vergani L, Dabbeni-Sala F. 1997. Quantification of muscle
917 mitochondrial oxidative phosphorylation enzymes via histochemical staining

918 of blue native polyacrylamide gels. Electrophoresis 18:2059-64.
919 61. Wittig I, Schägger H. 2005. Advantages and limitations of clear-native
920 PAGE. Proteomics 5:4338-46.
921 62. Webb MR. 1992. A continuous spectrophotometric assay for inorganic
922 phosphate and for measuring phosphate release kinetics in biological
923 systems. Proc Natl Acad Sci U S A 89:4884-7.
924 63. Zhang K. 2016. Gctf: Real-time CTF determination and correction. J Struct
925 Biol 193:1-12.
926 64. Pettersen EF, Goddard TD, Huang CC, Couch GS, Greenblatt DM, Meng
927 EC, Ferrin TE. 2004. UCSF Chimera--a visualization system for exploratory
928 research and analysis. J Comput Chem 25:1605-12.
929 65. Ando T, Kodera N, Takai E, Maruyama D, Saito K, Toda A. 2001. A high-
930 speed atomic force microscope for studying biological macromolecules. Proc
931 Natl Acad Sci U S A 98:12468-72.
932 66. Uchihashi T, Kodera N, Ando T. 2012. Guide to video recording of structure
933 dynamics and dynamic processes of proteins by high-speed atomic force
934 microscopy. Nat Protoc 7:1193-206.
935 67. Ngo KX, Kodera N, Katayama E, Ando T, Uyeda TQ. 2015. Cofilin-induced
936 unidirectional cooperative conformational changes in actin filaments
937 revealed by high-speed atomic force microscopy. eLife 4:e04806.
938

Figure 1

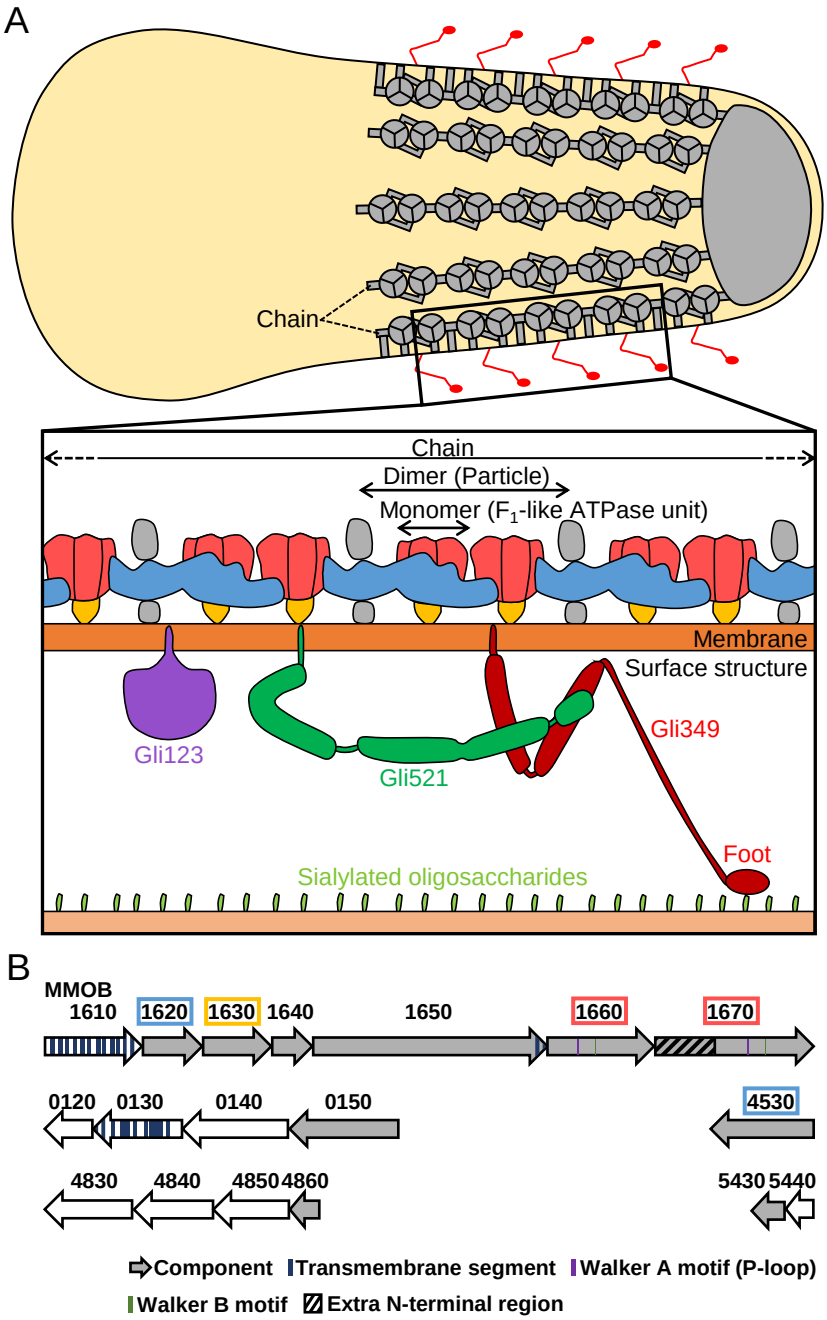
A
Chain
Chain
Dimer (Particle)
Monomer (F_1-like ATPase unit)
Membrane
Surface structure
Gli123
Gli521
Gli349
Foot
Sialylated oligosaccharides
B
MMOB
1610
1620
1630
1640
1650
1660
1670
0120
0130
0140
0150
4530
4830
4840
4850
4860
5430
5440
Component
Transmembrane segment
Walker A motif (P-loop)
Walker B motif
Extra N-terminal region

Figure 2

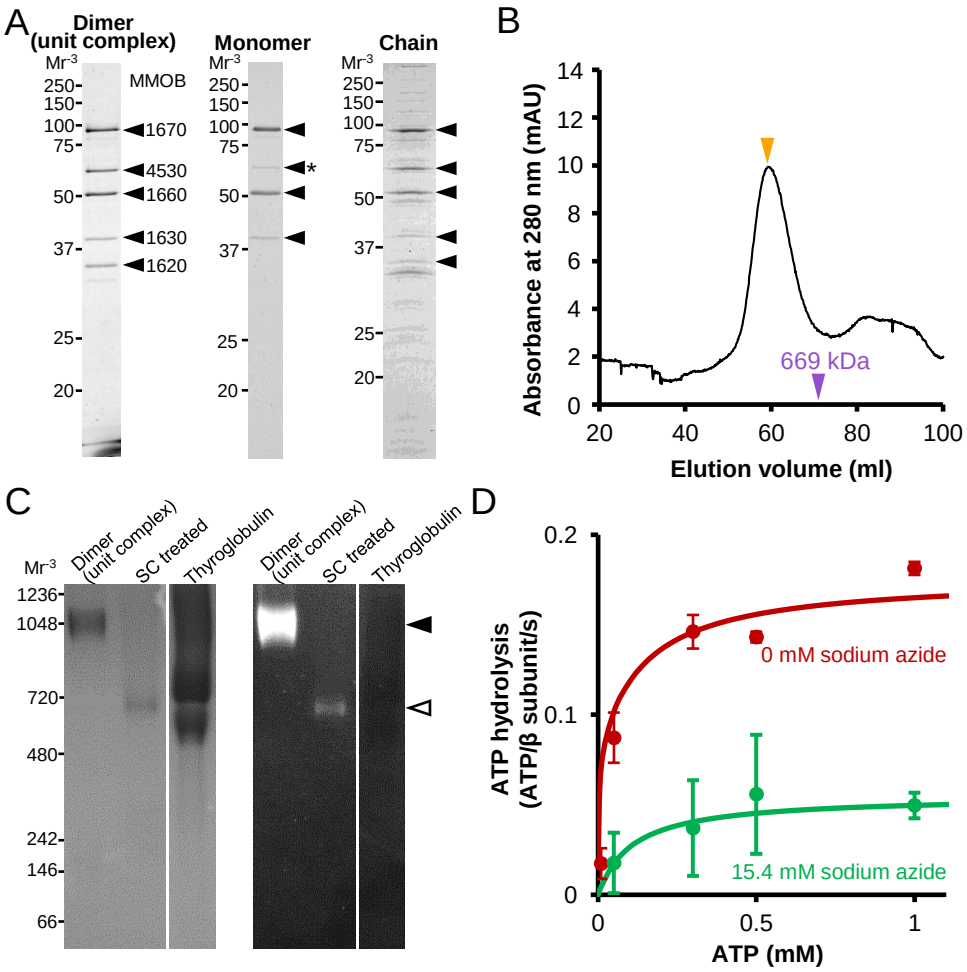
A
Dimer
(unit complex)
Monomer
Chain
Mr-3
MMOB
250
150
100
75
50
37
25
20
1670
4530
1660
1630
1620
*
B
Absorbance at 280 nm (mAU)
14
12
10
8
6
4
2
0
669 kDa
20
40
60
80
100
Elution volume (ml)
C
Mr-3
Dimer
(unit complex)
SC treated
Thyroglobulin
1236
1048
720
480
242
146
66
D
ATP hydrolysis
(ATP/β subunit/s)
0.2
0.1
0
0 mM sodium azide
15.4 mM sodium azide
0
0.5
1
ATP (mM)

Figure 3

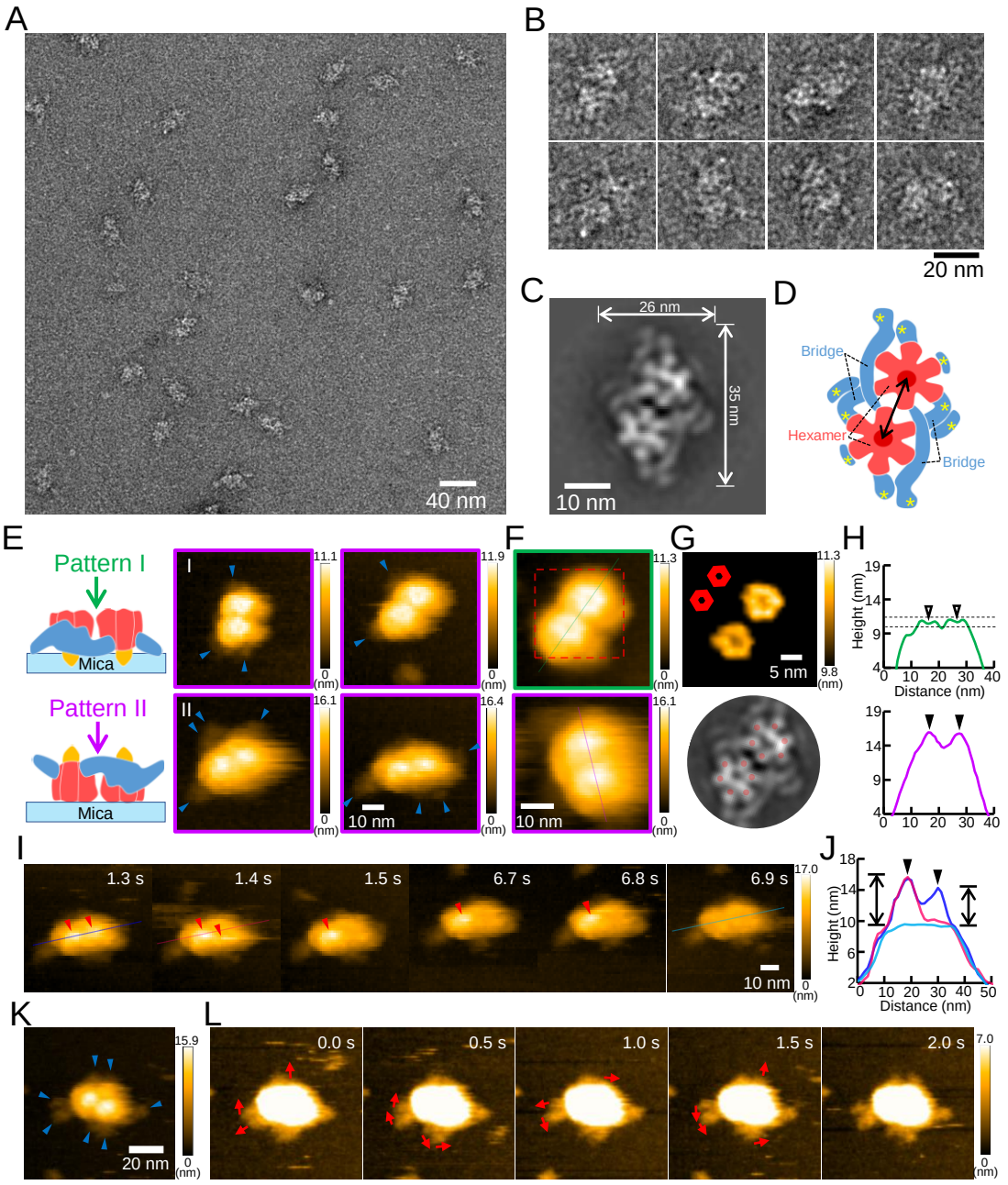
A
40 nm
B
20 nm
C
26 nm
35 nm
10 nm
D
Bridge
Hexamer
Bridge
E
Pattern I
Mica
Pattern II
Mica
I
II
10 nm
F
G
5 nm
H
Height (nm)
Distance (nm)
I
1.3 s
1.4 s
1.5 s
6.7 s
6.8 s
6.9 s
10 nm
J
Height (nm)
Distance (nm)
K
20 nm
L
0.0 s
0.5 s
1.0 s
1.5 s
2.0 s

Figure 4

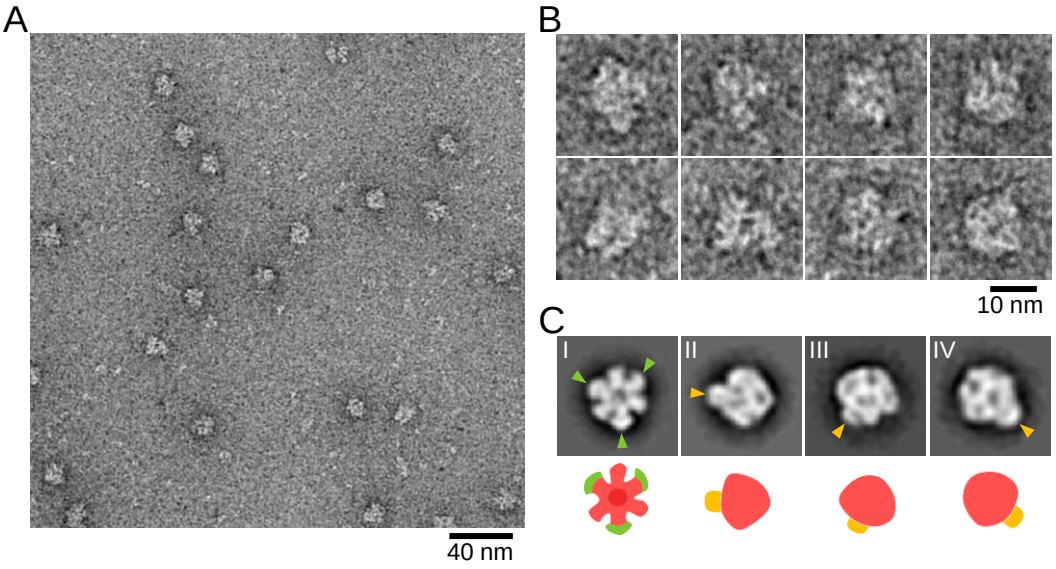

Figure 5

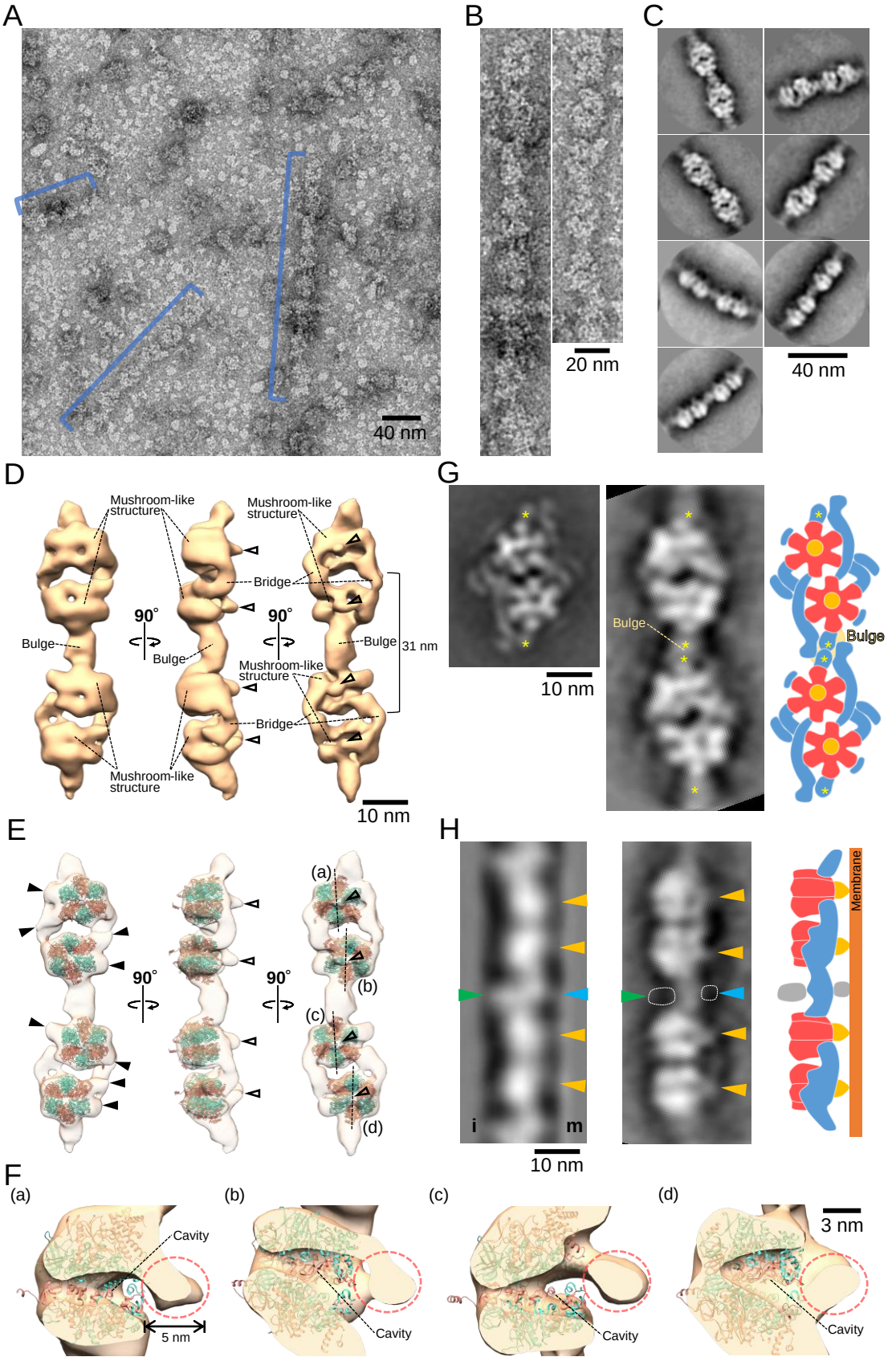
A
40 nm
B
20 nm
C
40 nm
D
Mushroom-like structure
Mushroom-like structure
Bridge
90°
90°
Bulge
Bulge
Bulge
31 nm
Mushroom-like structure
Bridge
Mushroom-like structure
10 nm
G
10 nm
Bulge
Bulge
E
90°
90°
(a)
(b)
(c)
(d)
H
i
m
10 nm
Membrane
F
(a)
(b)
(c)
(d)
Cavity
5 nm
Cavity
Cavity
3 nm
Cavity

Figure 6

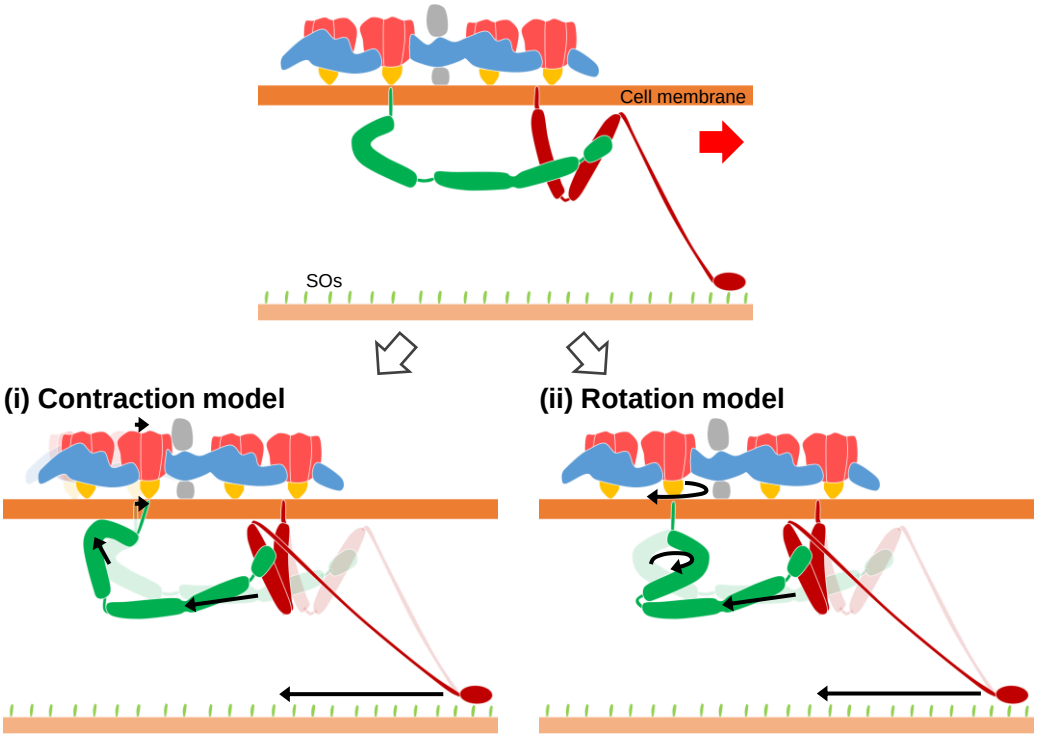

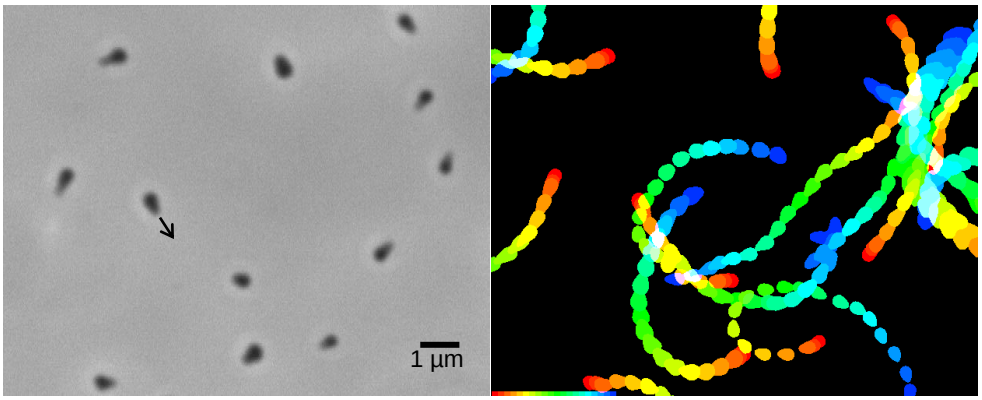

FIG S1 Gliding of *M. mobile* cells. Optical microscopy of cells (left) and trajectories of gliding cells (right). All cells are gliding in the direction of tapered end as indicated by a black arrow. For trajectories, video frames of every 0.2 s were colored differently from red to blue, and stacked for 4 s.

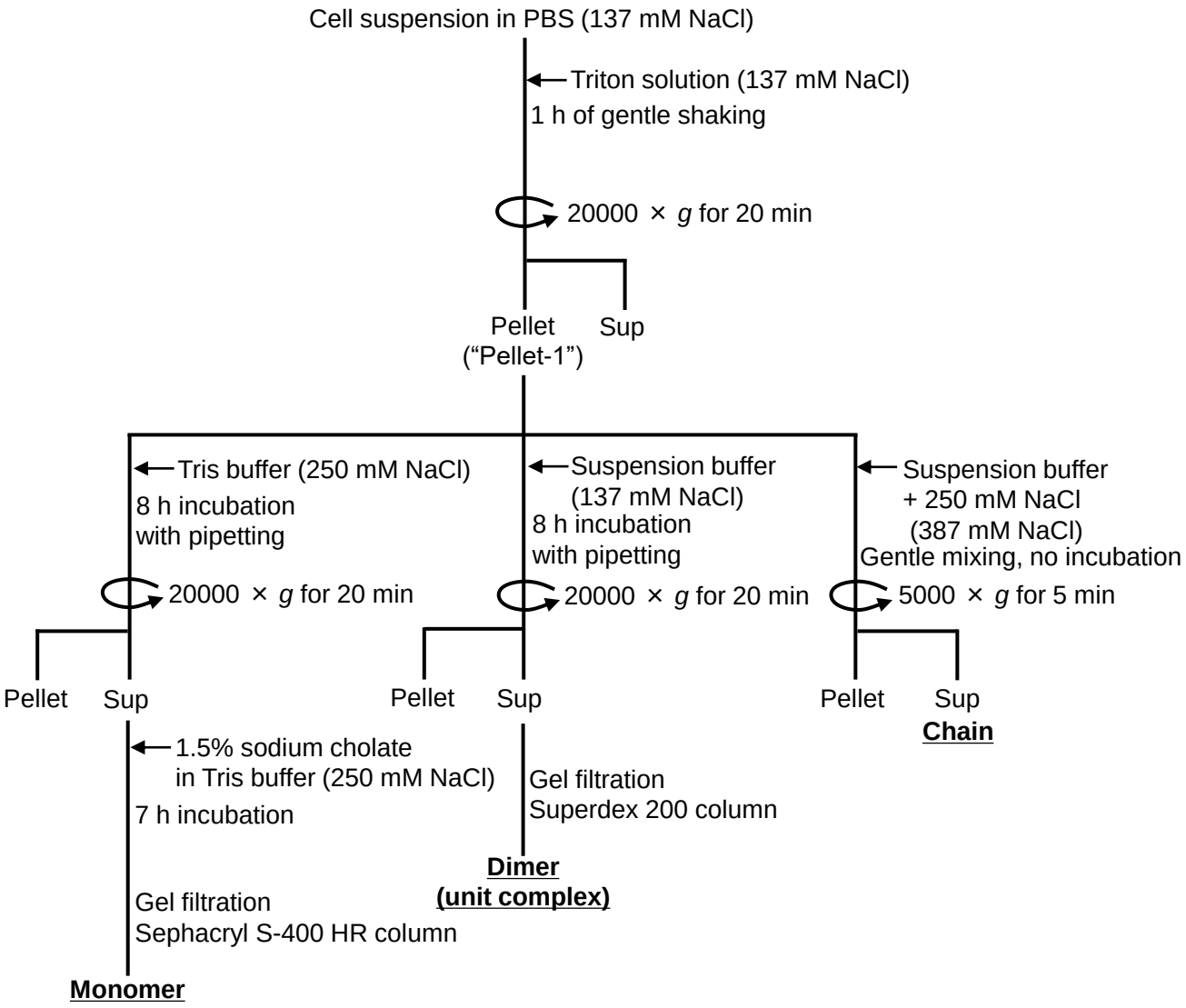

FIG S2 Isolation procedure for three fractions. Each fraction was obtained from Pellet-1 fraction. The adjusted concentrations of NaCl in the solution are indicated in parentheses. Supernatant is abbreviated as “Sup”. See Materials and Methods for details.

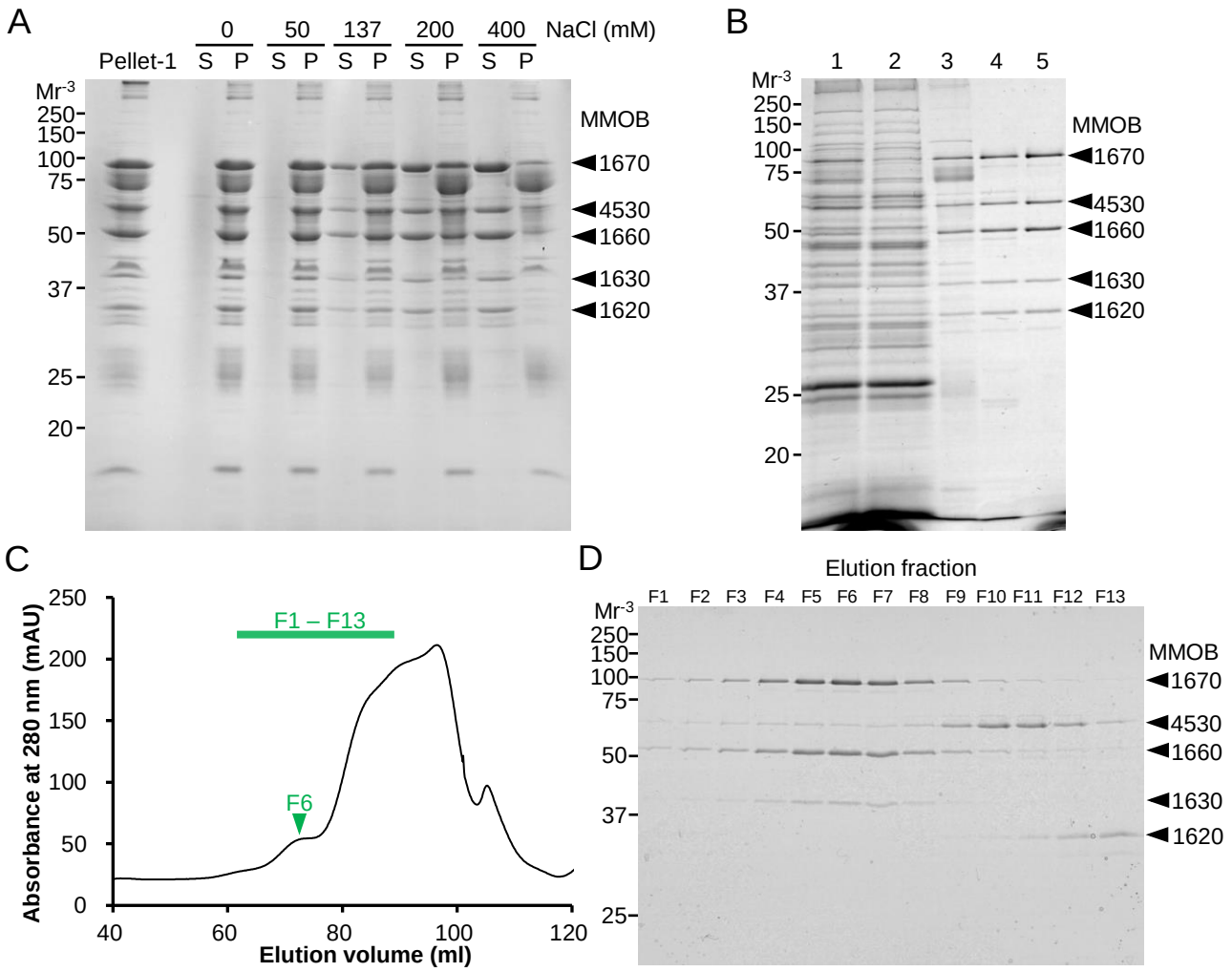

FIG S3 Isolation profile of Dimer (unit complex) and Monomer fractions. (A) Solubility of the chain components. Pellet-1 fraction was treated with buffers containing the specified concentrations of NaCl and centrifuged. Pellet-1 fraction, the supernatants (S) and the pellets (P) were analyzed by SDS-12.5% PAGE. See Materials and Methods for details. (B) Isolation of Dimer (unit complex). The fractions of each step were subjected to SDS-12.5% PAGE gel and stained with CBB. Lane 1, lysate of *M. mobile* cells; lane 2, Triton-soluble fraction; lane 3, Triton-insoluble (Pellet-1) fraction; lane 4, supernatant after incubation in suspension buffer containing 137 mM NaCl; lane 5, peak fraction of Superdex 200 gel filtration chromatography. The bands of Dimer components are marked by black triangles. (C) Gel filtration profile in Monomer isolation using a Sephacryl S-400 HR column. The small peak is marked by a green triangle. (D) The F1–F13 fractions in the gel filtration indicated by the green line in panel C were subjected to SDS-12.5% PAGE and stained with CBB. F6, which corresponds to the small peak in the gel filtration, was used for further analyses as Monomer fraction. Bands of Dimer components are marked by black triangles. For panels (A, B, D), Focused proteins were identified by PMF, and molecular masses are shown on the left.

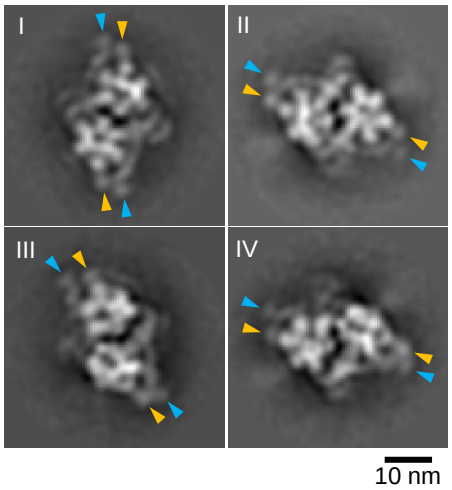

FIG S4 Two-dimensional averaged images of Dimer obtained by negative-staining EM. Four classes of clear particle images from 20 classes are represented. These images have common features as represented long and short protrusions marked by light blue and orange triangles, respectively. As mentioned in Fig. 3C, the images were mirrored to uniform handedness.

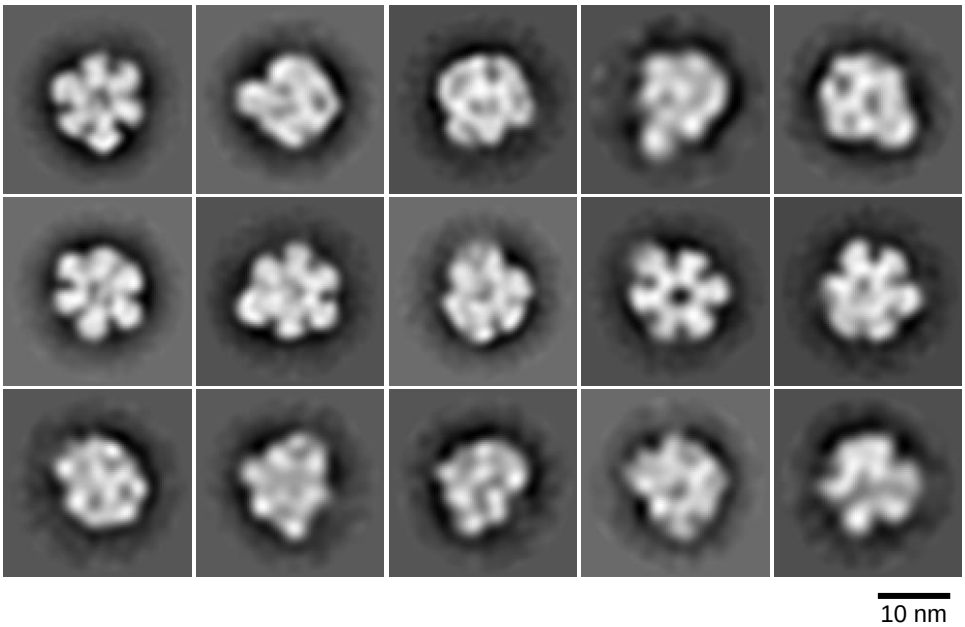

FIG S5 Two-dimensional averaged images of globular complex in Monomer fraction. Fifteen classes of clear particle images from 50 classes are represented.

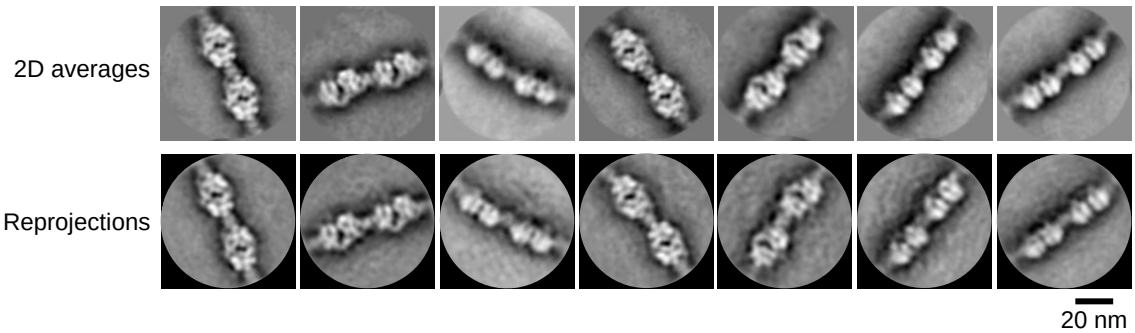

FIG S6 Reprojection images of Chain. Two-dimensional averaged images (upper) and the corresponding reprojection images (lower) calculated from the 3D map of Chain are compared.